2012

Statistical analysis of nanoparticles in optical confinement for biosensor application

Yi Hu
Lehigh University

Statistical analysis of nanoparticles in optical confinement for biosensor application

by

Yi Hu

A Dissertation
Presented to the Graduate Committee
of Lehigh University
in Candidacy for the Degree of
Doctor of Philosophy
in
Department of Physics

Lehigh University
September 2012

Approved and recommended for acceptance as a dissertation in partial fulfillment of the requirements for the degree of Doctor of Philosophy.
Student: Yi Hu
Dissertation Title: Statistical analysis of nanoparticles in optical confinement for biosensor application

---

Date

H. Daniel Ou-Yang, Dissertation Director, Chair

Accepted Date

Committee Members:

Xuanhong Cheng

James Gunton

Ivan Biaggio

Dimitrios Vavylonis

Dmitri Vezenov

Contents

List of Figures

Abstract

There is a growing interest in using dielectrophoretic, magnetic and optical forces to manipulate, concentrate and quantify nanoparticles such as dilute viral particles. Optical trapping, introduced by Ashkin in the early 1980s, is commonly used to control small species by light. However, technical challenges exist in studying the optically confined nanoparticles due to the small particle size, effects of Brownian motion, and the interparticle interaction in colloidal suspension. Fluorescence correlation spectroscopy (FCS) is well-known for its high sensitivity for measuring diffusion and concentrations of fluorescently labeled species. While it has been used successfully for suspensions in static and flow conditions, interpretation of the data obtained in the presence of a gradient potential has not been fully addressed.

Motivated by the above, this work addresses the theoretical and experimental issues that one needs to deal with when using FCS to analyze behavior of colloidal nanoparticles in an optical trap. We experimentally explore the potential and limitations of using FCS in a Gaussian potential. We interpret the results using Poisson statistics. For colloidal particles in an optical trap, even though the ambient concentration of nanoparticles can be low, the optical trapping can increase the local particle concentration, making particle interaction non-negligible. Both optical

trapping and particle interaction affect how FCS should be used for enumeration of optically confined nanoparticles. To demonstrate how FCS is affected by the Coulomb repulsion between colloidal particles, we use the grand canonical ensemble method to develop a general expression of the amplitude of the autocorrelation function that includes particle interaction.

After resolving the fundamental issues mentioned above, we use FCS to determine the concentration of a dilute suspension of HIV-1 virus-like particles in an optical trap. The trapping energy is determined for the virus-like particles and compared to the calculations using the discrete dipole approximation. To facilitate point-of-care applications for whole-particle sensing, an integrated opto-fluidic device that fluorescently labels particles for FCS detection has been designed and constructed.

With the framework established to deal with the use of FCS in the presence of optical trapping and particle interactions, this work has opened the door to virus sensing applications that use other concentrating methods such as electrophoresis and magnetic tweezers.

Chapter 1

Introduction

With the increasing interest in nanotechnology, great effort has been focused on the ability to manipulate nanoparticles via dielectrophoresis, magnetic forces, and optical tweezers [1–7]. For example, the concentration and quantification of dilute viral particles in suspensions are essential for early diagnosis of many diseases such as AIDS. Recent reports demonstrate the possibility of using dielectrophoresis or optical trapping methods to concentrate viral particles [7–9].

A possibility of controlling small particles by light was first introduced by Ashkin in the 1980s [10], who invented the optical tweezers, one of the most powerful and convenient tools for particle manipulation. In recent years, this technique has been extended to systems where an ensemble of nanoparticles is confined, called the optical bottle [11]. Even with a growing interest in studying the behavior of optically confined colloidal nanoparticles [12], technical challenges still exist here due to the small particle sizes, effects of Brownian motion, and the interparticle interactions in the colloidal suspensions.

Fluorescence correlation spectroscopy (FCS) [13–17] is one of the most sensitive techniques commonly used to study the dynamics and to evaluate the concentrations of fluorescently labeled species. This self-calibrated statistical analysis is associated with optical detection with high spatial and temporal resolution of the emitted fluorescence signal from a small number of molecules in a well-defined observation volume. FCS is famous for providing accurate quantitative information on transportation [18], diffusion [19] and interaction [20] of protein, as well as precise detection of dilute bio-molecules at low concentrations [15].

While FCS has been used successfully for suspensions in steady and flow conditions [21], interpretation of the data obtained in the presence of a gradient force produced by optical trapping has not been fully addressed. Osborne et al. [22] first examined the biased diffusion of molecules caused by optical trapping. Hosokawa et al. [23] utilized optically biased diffusion to study the formation of nanoparticle clusters. More recently, Wang et al. [24] studied the diffusion dynamics of gold nanoparticles in an optical gradient potential. Still, no analytical expression of FCS autocorrelation function has been reported for molecules in an optical confinement. Ito et al. [25] studied the effect of optical gradient force from a focused laser beam on FCS through Brownian dynamics simulation, and found that the conventional theoretical analytical expression of autocorrelation function, which is typically used to describe freely diffusing molecules, can be used to describe the behavior of molecules in a relatively shallow optical potential with trapping energies up to 1 k_BT. Meng et al. [26] in 2005 calculated the biased ACF numerically and compared it to Monte Carlo simulations of non-interacting particles in the presence of an isotropic trap.

They found good agreement between the initial amplitude $G(0)$ of the autocorrelation function and the number of particle in the trap, for trapping potentials lower than 2 k_BT.

This work focuses on a statistical analysis of colloidal systems in an optical confinement. I investigate the behavior of optically confined interacting particles via the bias of the initial amplitude of the autocorrelation function with respect to the particle number density. Using such approach, I theoretically and experimentally examine the limitations of FCS for determination of particle concentrations in the presence of a tightly focused laser beam, and in the presence of non-negligible particle interactions. In addition to the fundamental study, I demonstrate its applicability by designing and manufacturing an integrated opto-fluidic device that fluorescently labels bio-particles to enable FCS application.

In Chapter 2, I introduce the operating principles behind optical trapping and FCS, and provide a theoretical background for the techniques used in this work. In Chapter 3, I demonstrate the applicability of FCS to nearly ideal colloidal systems made of particles in an optical confinement, where particle interaction can be neglected. In Chapter 4, I demonstrate that optical trapping forces biases the FCS autocorrelation function, by verifying it experimentally. Chapter 5 has a focus on the application of the technique described in Chapter 3 on HIV-1 virus-like particles (VLPs). By determining the trapping energy of the VLPs, I provide an experimental guideline for future applications related to virus manipulations. Chapter 6 describes an opto-fluidic device I designed and constructed. This device consists of a microfluidic sample-processing chip for effective fluorescence labeling of particles, and an optical platform for enumerating particle concentration. In Chapter 7 gives global

conclusions and proposes future research directions in this field.

Chapter 2

Theoretical background

In this chapter, I introduce the physical principles behind the optical trapping and fluorescence correlation spectroscopy. Then, analytical calculations of the FCS autocorrelation function for particles in a trapping potential will be discussed.

2.1 Optical trapping

2.1.1 Physics behind of the optical trapping

For decades, much scientific effort is devoted to understanding the light-matter interaction: matter can modify the flow of light, while light can exert forces on matter. A possibility of controlling small particles by light was first introduced by Ashkin in the 1980s [10], who invented the optical tweezers, one of the most powerful and convenient tool for optical manipulation of particles. Optical tweezers consist of a tightly focused laser light that acts like an optical trap, which confines small

particles in the intensity maximum of the beam. There are two types of forces acting on the particles in an optical trap: a gradient force that attracts a particle to the laser focus, and a scattering force in the direction of the light propagation caused by the absorption and scattering of photons by the dielectric particles.

The operation of optical tweezers for particles with diameters sufficiently larger than the wavelength of the light can be successfully described classically: Rays of light made of photons that carry momentum and that are bent by refraction when passing through a dielectric sphere with a refractive index different from the surrounding medium. To satisfy the conservation of total momentum, the net change of momentum in the deflected rays equals to the net change in momentum of the dielectric sphere. When this dielectric sphere finds itself in the gradient of the laser light intensity, it experiences an imbalance of forces that tend to push the sphere towards the region of higher intensity in the laser beam.

Naturally, geometrical optics poorly describes the light intensity in the vicinity of the laser focus, and neglects effects of diffraction. Hence, it is not applicable for particles that are much smaller compare to the wavelength ($d \ll \lambda$). A better description is achieved when particles are considered as point dipoles that interact with the electro-magnetic field in the vicinity of the laser focus.

A sphere with radius r placed in a homogeneous electric field $\vec{E}$ acquires an induced dipole moment,

$$\vec{p}_{dipole} = 4\pi n_m^2 \varepsilon_0 r^3 \left(\frac{m^2 - 1}{m^2 + 2} \right) \vec{E}, \tag{2.1}$$

where $m = n_p/n_m$ is the relative refractive index of particle to the medium, n_p and

n_m are the refractive indices of a particle and of a medium.

For small particles placed in an electric field with intensity $I(\vec{r})$, the gradient force due to non-uniform intensity distribution can be written as [27]

$$\vec{F}_{grad} = \frac{2\pi n_m r^3}{c}\left(\frac{m^2-1}{m^2+2}\right)\nabla\vec{I} \tag{2.2}$$

Further, the scattering force can be expressed as:

$$\vec{F}_s = n_m\frac{\sigma\left\langle\vec{S}\right\rangle}{c} = \frac{8\pi}{3}\frac{n_m k^4 r^6}{c}\left(\frac{m^2-1}{m^2+2}\right)^2 I, \tag{2.3}$$

where σ is the scattering cross section, $\langle\vec{S}\rangle$ is the time averaged Poynting vector and k is the wavenumber.

For small particles whose diameter is less than the light wavelength (Rayleigh regime), the scattering force is proportional to the light intensity, while the gradient force is proportional to intensity gradient. Assuming a paraxial Gaussian beam, the stability condition for a particle (far from the absorption resonance) is given by the ratio of the gradient force to the scattering force that scales as

$$\left|\frac{F_{grad}}{F_{scat}}\right| \propto \frac{\lambda_0^4 z_0}{a^3 r_0^2} \gg 1 \tag{2.4}$$

where w_0 is the beam waist of the trapping beam, z_0 is the Rayleigh range, and r_0 is the radius of particle.

Therefore, for the trapping of small particles, the scattering force is commonly ignored. Although it appears that small particles are easier to be trapped comparing

to large ones, in reality it is not the case, because of the additional contribution caused by the Brownian motion of the particles. The thermal energy associated with the Brownian motion is k_BT, with the Boltzmann constant k_B and temperature T. This energy has to be compared with the depth of the trapping potential U_{trap}, generated by the conservative gradient force (by integration of Eq. 2.2):

$$U_{trap} = -\frac{2\pi n_m r^3}{c}\left(\frac{m^2-1}{m^2+2}\right) I + C \tag{2.5}$$

where C is an arbitrary constant. The drag force due to the dynamic viscosity η is $F_{drag} = -6\pi\eta r v$ for a spherical particle with radius r and velocity v, it decreases with increasing radius r, thus efficiently damps the Brownian motion.

2.1.2 Numerical calculation of the optical force spectra: Discrete dipole approximation (DDA)

As mentioned earlier, in cases where the diameter of a trapped particle is significantly smaller than the wavelength of the light $d \ll \lambda$, the condition for Rayleigh scattering is satisfied, and the particle is treated as a point dipole in an inhomogeneous electromagnetic field.

Conventionally, in Mie theory, the electromagnetic field is expanded into a series of spherical harmonic functions. Both the electromagnetic field inside and outside the sphere is taken to satisfy the boundary conditions. With a given incident field, the scattering field can be calculated by solving Maxwell's equations under the

boundary conditions. However, if the particle has a complex shape such as non-spherical particle or multi-layered particle, the Mie theory is not convenient to use.

Alternatively, the discrete dipole approximation (DDA) is effective when dealing with nanometer- to micrometer-sized dielectric particles with arbitrary geometric shapes and refractive indices. It can be efficiently used to compute the optical forces on a particle placed anywhere around the focus of a Gaussian beam. [28]

2.2 Fluorescence correlation spectroscopy (FCS)

2.2.1 Background

Fluorescence correlation spectroscopy (FCS) [13–17,29] is a statistical analysis of the emitted fluorescence from a small number of molecules in a well-defined observation volume (on the order of femtoliter), that has high spatial and temporal resolution. In contrast to other sensitive techniques such as *atomic force microscopy* or *fluorescence microscopy*, the outstanding feature of FCS is that the parameter of primary interest is not the emission intensity itself, but rather the intensity fluctuations caused by the deviation of the small system from thermal equilibrium. By self-correlating the deviations of emitted fluorescence intensity created by the Brownian motion of the particles in and out of the observation volume, FCS can provide quantitative information about the particles, such as the average concentration and diffusion dynamics.

Fluorescence correlation spectroscopy was introduced by Madge, Elson and Webb in 1972 [13], through measurements of diffusion and chemical dynamics of DNA-drug

intercalation. This pioneer work has been followed by a number of studies that determined particle concentration [15], translational and rotational mobilities in two and three dimensions in flow systems, or even in the cellular environment [30, 31]. However, the early studies suffered from low signal-to-noise ratios because of low detection efficiencies, and insufficient background suppression. It was not until the 1990s that FCS was combined with *Confocal microscopy* to achieved a revolutionary improvement of FCS. Modern FCS setups commonly include a stable laser source, sensitive detectors, (such as avalanche photodiodes with single-photon sensitivity, or photomultiplier tubes), and confocal optics configuration. The incoming laser light is strongly focused by a powerful objective with high numerical aperture ($NA > 0.9$) to a diffraction limited spot, hence, only a few fluorophores within the illuminated region are present. In order to limit the detection volume also in the axial direction, a pinhole is introduced in the image plane, which blocks all light that is not coming from the focal region. Because the detection volume is limited to less than one femtoliter, single particle "resolution was achieved. A schematic illustration of an FCS setup is shown in Fig. 2.1. Recently, with the development of the two-photon excitation technique, the excitation volume is further reduced, and signal-to-noise ratio can be greatly improved.

2.2.2 Point spread function in confocal microscopy

The principle of confocal imaging was first introduced by Marvin Minsky in 1957. In conventional microscopy, a large volume can be flooded with light and simultaneously excited and detected by the photodetector or camera. Conversely, confocal

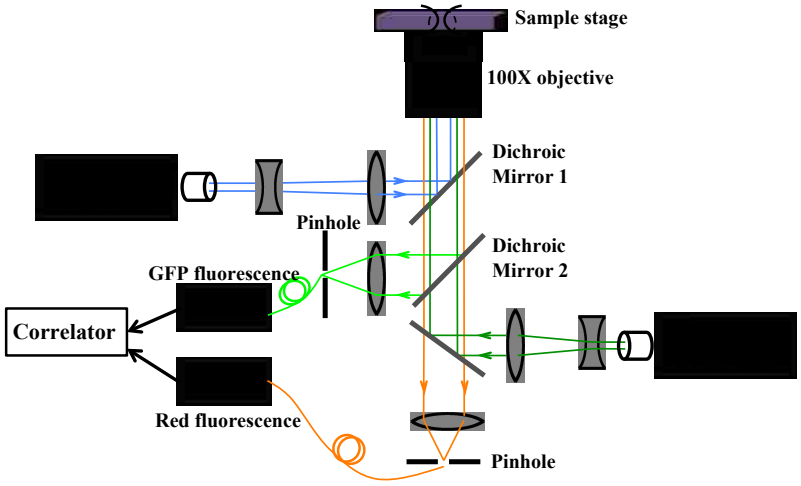

Figure 2.1: A typical FCS setup containing two laser sources and two detectors.

microscopy is an optical imaging technique that can be used to increase optical resolution and contrast by using point illumination and a spatial pinhole to eliminate out-of-focus light from detection.

The small excitation and detection volume that is involved in this configuration allows efficient detection of fluorescence intensity fluctuations. When quantifying the relationship between the detected signal and the spatial intensity distribution of the emitting sample, one needs to take into account the point spread function (PSF) of the imaging. A scaled PSF normalized to the origin can be defined as:

$$\overline{PSF}\,(x,y,z) = \frac{PSF\,(x,y,z)}{PSF\,(0,0,0)} \tag{2.6}$$

The PSF relevant to confocal microscopy is given by the convolution of the excitation PSF and the detection PSF, and has been described in detail [32]. It was shown that effective PSF can be well approximated by a three-dimensional Gaussian

(3DG) [33].

$$\overline{PSF}_{3DG}(x,y,z) = \frac{I(x,y,z)}{I_0} = exp\left[-\frac{2(x^2+y^2)}{w_0^2} - \frac{2z^2}{z_0^2}\right], \tag{2.7}$$

where w_0 and z_0 were defined by Rigler and Mets [20] as:

$$w_{theory} \geq \frac{\lambda}{n\pi \tan(\alpha/2)} \tag{2.8}$$

$$z_{theory} \approx \frac{es_0}{\tan(\alpha)} \times 0.72 \tag{2.9}$$

where $\alpha = \arcsin(NA/n)$, NA is the numerical aperture of the objective, n is the refractive index of the specimen, s_0 is the pinhole radius divided by the magnification.

2.2.3 Poisson statistics of diffusing molecules

Molecular motion is often described as stochastic behavior driven by thermal fluctuation, commonly referred to as Brownian motion. In the stochastic theory, the molecules in a solution are represented by discrete objects on imaginary lattices. The transition probability between lattices are defined according to the mobility properties of the molecules. The concentration gradient of a dissolved substance is described by Fick's laws.

The definition of concentration C of a species in suspension is the ratio of the total particle number N_{total} and the total volume V_{total}. When going to a very small volume where the number of particles is low, the spatial fluctuation of the local

particle density occurs. The distribution of the particle number N in a small sub-volume V follows a Poissonian distribution with the mean particle number $\mu = N$:

$$P\left(n, \mu = N\right) = \frac{N^n}{n!} e^{-N} \tag{2.10}$$

The fluctuation of the number density is then given by its variance $Var\left(N\right) = \langle \Delta N^2 \rangle$. The relative fluctuation of a number counting experiment is given by:

$$\frac{\sqrt{Var\left(N\right)}}{\langle \Delta N \rangle} = \frac{1}{\sqrt{\langle \Delta N \rangle}} \tag{2.11}$$

2.2.4 Theory of autocorrelation function

For Poisson processes such as diffusion, the variance of the fluctuation in a parameter equals the average parameter value, that is

$$\langle \Delta N^2 \rangle = \langle N \rangle \tag{2.12}$$

For parameters such as concentration C, and fluorescence intensity F, which are directly proportional to N, we can write,

$$\frac{\langle \Delta N^2 \rangle}{\langle N \rangle^2} = \frac{\langle \Delta C^2 \rangle}{\langle C \rangle^2} = \frac{\langle \Delta F^2 \rangle}{\langle F \rangle^2} = \frac{1}{\langle N \rangle} \tag{2.13}$$

A typical FCS experiment measures the autocorrelation function $G(0)$ of the fluorescence intensity detected from a volume around the focus of a laser beam.

The autocorrelation function $G(\tau)$ is defined as:

$$G(\tau) = \frac{\langle \delta F(t) \cdot \delta F(t+\tau) \rangle}{\langle F(t) \rangle^2}, \tag{2.14}$$

where τ is the correlation delay time, F(t) is the instantaneous fluorescence intensity at time t, and δF(t) = F(t) − ⟨F(t)⟩ is the fluctuation of the fluorescence intensity around its mean value.

The fluctuation of the collected fluorescence can be written as:

$$\delta F(t) = \int_V \overline{PSF}(\vec{r})\, \delta\left(C(\vec{r}, t)\right) dV \tag{2.15}$$

where $\overline{PSF}$ is the point spread function for the emitted light that has a three-dimensional Gaussian distribution; $C(\vec{r}, t)$ is the local concentration at time t.

By substituting Eq. 2.15 into Eq. 2.14, we can re-write it as:

$$G(\tau) = \frac{\int\int \overline{PSF}(\vec{r})\, \overline{PSF}(\vec{r}')\, \langle \delta C(\vec{r}, 0)\, \delta C(\vec{r}', \tau) \rangle\, dV dV'}{\left(\langle C \rangle \int \overline{PSF}(\vec{r})\, dV\right)^2} \tag{2.16}$$

For particles that are freely diffusing in three dimensions with the diffusion coefficient D, the diffusion equation describes the temporal and spatial evolution of a concentration distribution as:

$$\frac{\partial C(\vec{r}, t)}{\partial t} = D \Delta C(\vec{r}, t) \tag{2.17}$$

Assuming an initial point-like distribution of molecules with concentration $C(x, t_0) =$

$\delta(x - x_0)$, the solution of Eq. 2.17 is given by:

$$\left\langle \delta C(\vec{r}, 0)\, \delta C\left(\vec{r'}, \tau\right) \right\rangle = \langle C \rangle (4\pi D\tau)^{\frac{3}{2}} \cdot \exp\left[-\frac{\left(\vec{r} - \vec{r'}\right)^2}{4D\tau} \right] \tag{2.18}$$

Thus, Eq. 2.16 yields:

$$\begin{aligned} G(\tau) &= \frac{\int\int \overline{PSF}(\vec{r})\, \overline{PSF}(\vec{r'}) \cdot \exp\left[-\frac{(\vec{r} - \vec{r'})^2}{4D\tau} \right] dV dV'}{\left(\langle C \rangle \int \overline{PSF}(\vec{r})\, dV \right)^2} \\ &= \frac{(4\pi D\tau)^{\frac{3}{2}}}{\langle C \rangle} \frac{\int\int \overline{PSF}(\vec{r})\, \overline{PSF}(\vec{r'})\, \langle C \rangle (4\pi D\tau)^{\frac{3}{2}} \cdot e^{-\frac{(\vec{r} - \vec{r'})^2}{4D\tau}} dV dV'}{\left(\int \overline{PSF}(\vec{r})\, dV \right)^2} \end{aligned} \tag{2.19}$$

Here we define the lateral diffusion time τ_D that a molecule stays in the focal volume in terms of the diffusion coefficient D as follow:

$$\tau_D = \frac{w_0^2}{4D} \tag{2.20}$$

And the effective focal volume V_{eff} as:

$$V_{eff} = \frac{\left(\int \overline{PSF}(\vec{r})\, dV \right)^2}{\int \overline{PSF}^2(\vec{r})\, dV} = \pi^{\frac{3}{2}} \cdot r_0^2 \cdot z_0 \tag{2.21}$$

Finally, the calculated autocorrelation function for a non-interacting, freely diffusing, point-like species of molecules in solution can be written as:

$$G(\tau) = \frac{\langle \Delta N^2 \rangle}{\langle N \rangle^2} \left(1 + \frac{4D\tau}{w_0^2} \right)^{-1} \left(1 + \frac{4D\tau}{z_0^2} \right)^{-1/2} \tag{2.22}$$

where D is the diffusion coefficient of the particles, ω_0, z_0 are the radial and axial dimensions of the detection volume, respectively, and $\langle N^2 \rangle$, $\langle N \rangle$ are the varience and the mean number of particles in the volume, respectively [14]. The amplitude of the autocorrelation function at zero lag time G(0) is the normalized variance of the particle number fluctuations $\langle \Delta N^2 \rangle / \langle N \rangle^2$. When the probability of finding a particular particle in the laser focus is $\ll 1$, the number fluctuation of particles in this region follows a Poisson distribution. In this case the variance of the distribution $\langle \Delta N^2 \rangle$ equals to the mean number density $\langle N \rangle$ [14], and the prefactor in Eq. 2.22 simplifies to

$$G(0) = \langle N \rangle^{-1} \tag{2.23}$$

2.3 Autocorrelation function for molecules in a harmonic potential

To have a better understanding of the dynamics of nanoparticles in an optical trap, it is necessary to develop a suitable model for the biased ACF in an optical trap. To solve the Eq. 2.14, one first needs to solve for the propagator in the potential from Fokker-Planck equation.

$$\frac{\partial}{\partial t} C(\vec{r}, t) = \frac{\partial}{\partial t} \left[D(r) \nabla C(\vec{r}, t) - F(\vec{r}, t) C(\vec{r}, t) \right] \tag{2.24}$$

where $C(\vec{r}, t)$ is the concentration distribution we are interested in, $D(\vec{r})$ is the diffusion coefficient, and $F(\vec{r}, t)$ is the force profile over space and time.

As we discussed in chapter 2.1, the optical trapping forces in the laser focus have

complex forms. To avoid the complexity, we first consider a simplified model of trapping potential, 3-dimensional harmonic potential $U = \frac{1}{2}kr^2$, with homogeneous forces $F(x,t) = -kx$. Two reasons for choosing this model are, (1) the optical potential at the central region of the trap is commonly estimated as a harmonic potential; (2) the solution to Eq. 2.24 for such a model has been already established. The propagator which describes the probability that a particle diffuses from $\vec{r}$ to $\vec{r}'$ in time period t can be written as:

$$P\left(\vec{r},\vec{r}';t\right) = \left[\frac{2\pi k_B T}{k}\left(1-\exp\left(-2t/\tau\right)\right)\right]^{-3/2} \times \exp\left[-\frac{k\left[\vec{r}-\vec{r}'\exp\left(-t/\tau\right)\right]^2}{2k_BT\left[1-\exp\left(-2t/\tau\right)\right]}\right] \tag{2.25}$$

There are two limiting cases: (1) When t is small, $t \ll \tau$, $P\left(\vec{r},\vec{r}';t\right)$ is the same as for free diffusion:

$$P\left(\vec{r},\vec{r}';t\right) = (4\pi Dt)^{-3/2}\exp\left[-\frac{\left(\vec{r}-\vec{r}'\right)^2}{4Dt}\right] \tag{2.26}$$

(2) When t is large, $t \gg \tau$, $P\left(\vec{r},\vec{r}';t\right)$ becomes the Boltzmann distribution,

$$P\left(\vec{r},\vec{r}';t\right) = \left(\frac{k}{2\pi k_BT}\right)^{3/2}\exp\left[-\frac{k}{2k_BT}r^2\right] \tag{2.27}$$

For the first case, the autocorrelation function will be the same as Eq. 2.22 for free diffusive particles. However, for the second case, the autocorrelation function will be very different. To calculate the autocorrelatioin function for optically trapped

particles, we substitute the probability distribution (Eq. 2.27) into Eq. 2.16.

$$G(t) = \frac{1}{\pi^{3/2} r_0^2 z_0 \langle C \rangle} \cdot \frac{1}{\left(\frac{1+e^{-2^{t/\tau}}}{2} + \tau D \cdot \frac{2\left(2-e^{-2^{t/\tau}}\right)}{r_0^2} \right)} \cdot \frac{1}{\sqrt{\frac{1+e^{-2^{t/\tau}}}{2} + \tau D \cdot \frac{2\left(2-e^{-2^{t/\tau}}\right)}{z_0^2}}} \tag{2.28}$$

Since the effective volume can be expressed as $V_{eff} = \pi^{3/2} r_0^2 z_0$, the ACF can be simplified to:

$$G(t) = \frac{1}{\langle N \rangle} \cdot \frac{1}{\left(\frac{1+e^{-2^{t/\tau}}}{2} + \tau D \cdot \frac{2\left(2-e^{-2^{t/\tau}}\right)}{r_0^2} \right)} \cdot \frac{1}{\sqrt{\frac{1+e^{-2^{t/\tau}}}{2} + \tau D \cdot \frac{2\left(2-e^{-2^{t/\tau}}\right)}{z_0^2}}} \tag{2.29}$$

For the case that $t \to 0$, we obtain $G(0) = \frac{1}{\langle N \rangle}$, the same result as the case for free diffusing particles.

2.4 Mean particle number in a Gaussian potential

When complex forces such as optical gradient forces are involved, no analytical solution for autocorrelation function exists. Numerically, Meng et al. derived a solution [26] for this case. To avoid the complexity in the dynamics of the nanoparticles in a Gaussian potential, one can calculate the mean number of particles in the trap N_{trap}, assuming that the intensity distribution of the beam at the laser focus

has a three-dimension Gaussian shape:

$$W(r,z) = \exp(-\frac{2r^2}{w_0^2} - \frac{2z^2}{z_0^2}) \tag{2.30}$$

where w_0 and z_0 are the radial and axial beam waists, respectively.

The gradient potential due to such an intensity distribution is:

$$U(\vec{r}) = -\frac{\alpha P W(\vec{r})}{\pi \varepsilon_0 c n_m w_0^2} \tag{2.31}$$

where α, P, ϵ_0, c and n_m represent the polarizability of the particle, the laser power, the dielectric constant of vacuum, the speed of light in vacuum and the refractive index of the medium, respectively.

When the system reaches equilibrium, the concentration can be calculated from the Boltzmann distribution

$$C(\vec{r}) = C_0 \exp(U(\vec{r})/k_B T) = C_0 \exp(\beta W(\vec{r})), \tag{2.32}$$

where

$$\beta = \frac{\alpha P}{\pi \varepsilon_0 c n_m w_0^2 k_B T} = \frac{U(0)}{k_B T} \tag{2.33}$$

is a dimensionless factor that measures the peak strength of the gradient field energy relative to thermal energy.

Assuming that the detection volume of FCS also has a three-dimensional Gaussian distribution with the same beam waists as the excitation beam, the average

number of particles in the excitation volume can be expressed as:

$$N_{trap} = \int C(\vec{r})W(\vec{r})d^3\vec{r} \tag{2.34}$$

Substituting Eq. 2.32 into the Eq. 2.34, the number density enhancement due to the trapping can be written as:

$$\frac{N_{trap}}{N_0} = \frac{\int C_0 \exp(\beta W(\vec{r}))W(\vec{r})d^3\vec{r}}{\int C_0 W(\vec{r})d^3\vec{r}} \tag{2.35}$$

where N_{trap} and N_0 correspond to the average particle numbers in the detection volume with and without the gradient field. Substituting Eq. 2.30 and Eq. 2.33 into Eq. 2.35, one can obtain a numerical solution of the equation above.

Chapter 3

Fluorescence correlation spectroscopy of ideal-gas-like nanoparticles in an optical trap

Being one of the most sensitive techniques to detect molecules and nanoparticles in solution, fluorescence correlation spectroscopy (FCS) is used routinely to describe molecular diffusion of fluorescent species in a well-defined detection volume created by a tightly focused laser beam. However, the use of FCS in a gradient field should be considered with caution because the gradient force near the center of the laser focus can affect both the concentration and diffusion dynamics of the confined nanoparticles in the confinement. Osborne et al. [22] first discussed the biased diffusion of molecules caused by optical trapping and its effect on FCS. Hosokawa et

al. [23] utilized such optically biased diffusion to study the formation of nanoparticle clusters. More recently, Wang et al. [24] studied the diffusion dynamics of gold nanoparticles in an optical gradient potential. Yet, no analytical expression of the FCS autocorrelation function (ACF) is reported for confined molecules in an optical gradient. Ito et al. [25] studied the effect of optical gradient force from a focused laser beam on FCS through Brownian dynamics simulation, and found that the conventional theoretical analytical expression of ACF (Eq. 2.22, page 17), which typically is used to describe free diffusing molecules, can be used to describe the behavior of molecules in a relatively shallow optical force potential up to 1 k_BT. Meng et al. [26] in 2005 calculated the biased ACF numerically and compared it to the Monte Carlo simulations of non-interacting particles in the presence of an isotropic trap (sphere shaped). They found good agreement between the amplitude of ACF $G(0)$ and the particle number in the trap for trapping potentials lower than 2 k_BT.

In this chapter, I described experiments performed in a nearly ideal system where interaction between particles can be neglected, to test the theoretical predictions by Meng et al. [26] and Ito et al. [25]. I investigate the relation $G(0) = 1/\langle N \rangle$ (Eq. 2.23) for dilute suspension of particles in an optical trapping potential, where $\langle N \rangle$ is the mean number of particles in the trap.

3.1 Experimental setup

Fig. 3.1 shows the experimental setup for this experiment. A continuous wave (CW) laser (1064 nm) is used to trap fluorescent nanoparticles, while a CW argon laser

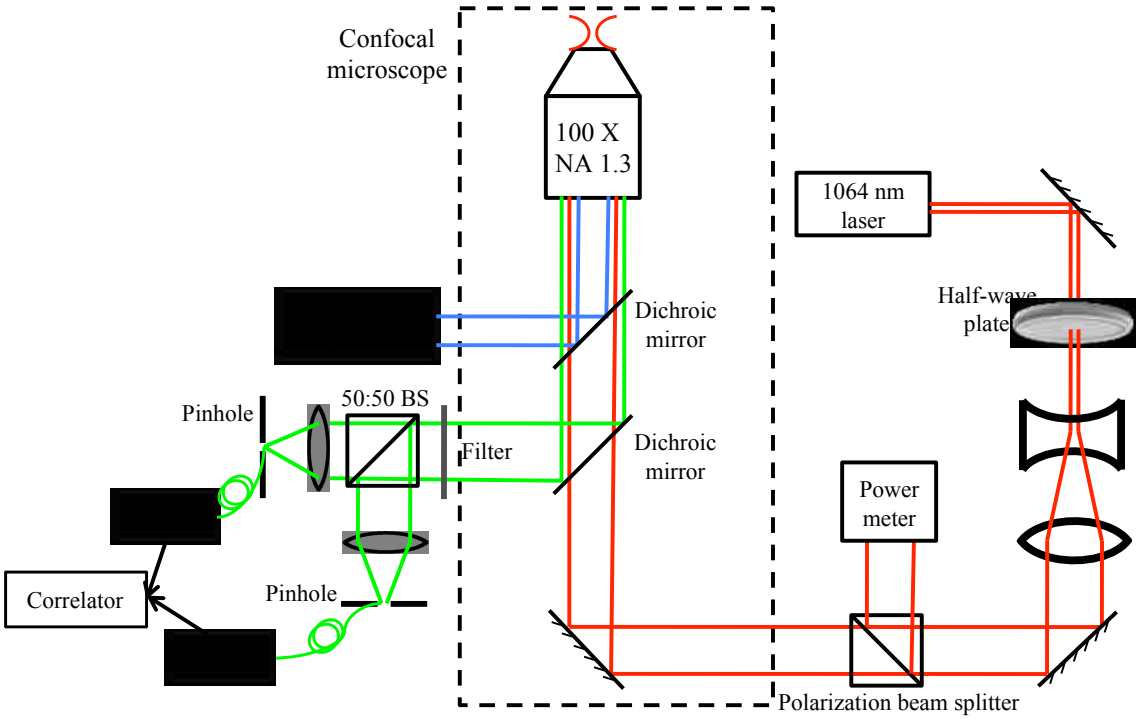

Figure 3.1: Schematics of the experimental setup. The FCS excitation laser (wavelength at 488 nm) is confocally aligned with the trapping laser (wavelength at 1064 nm). The focal volume of the 488 nm laser is roughly $\frac{1}{10}$ that of the 1064 nm laser.

at wavelength 488 nm was used to excite the fluorophores. The IR laser power is adjusted by changing the orientation of a half-wave plate relative to the linear polarizer. In order to achieve a Gaussian intensity distribution at the laser focus, the trapping laser beam is expanded to slightly overfill the back aperture of the 100× objective (PlanFluor 100× N.A.=1.3, Olympus) [34]. The two laser beams are merged using a dichroic mirror (see Fig.ẽffig:TrappingSetup). A microscope objective is used to both focus the two laser beams, and to collect the emitted fluorescence. The fluorescence emission that passes through a band-pass filter is divided into two equal portions by a beam splitter, and each beam is then collected

by a photon-counting avalanche photodiode (APD) (SPCM-AQRH-13-FC Perkin Elmer). The cross-correlation functions of the APD outputs are obtained by a correlator (Flex02-01D, Correlator.com).

3.2 Sample preparation

An aqueous suspension of 110 nm polystyrene spheres labeled with fluorescent Firefli red (excitation maximum at 543 nm, emission maximum at 612 nm, Fisher Scientific) is diluted to a volume fraction of 0.01% by deionized water. At excitation laser power used (about $10\,\mu W$), no photo-bleaching is observed. The estimated ionic strength is $10\,\mu M$. The fluorescence photon counts measured through APDs are verified to be linearly proportional to the average number of particles in the observation volume. A $20\,\mu L$ sample was sandwiched between a cover-glass and a standard microscope slide, and is sealed with wax (shown in Fig. 3.2). The gap between the two substrates is estimated to be 50 to $70\,\mu m$.

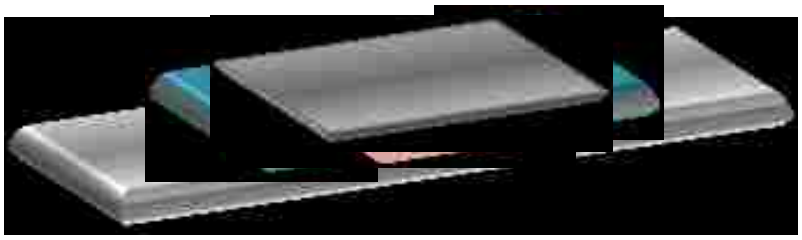

Figure 3.2: Illustration of the sample chamber.

3.3 System calibration of FCS

The autocorrelation curve of the fluorescence intensity is calculated from Eq. 2.14, and fitted with Eq. 2.22. There are four unknown parameters that lie inside of Eq. 2.22: the average number of particles in the observation volume $\langle N \rangle$, the diffusion coefficient D of the species in suspension, the beam waist of laser w_0 and the shaping parameter $S = z_0/w_0$. In this section, I will describe the experimental calibration of the three parameters $\langle N \rangle$, V_{eff}, and D, as determined by FCS.

3.3.1 Calibration of mean particle number

First, to verify an assumption that the excitation laser beam does not introduce any additional trapping, I performed an experiment with the same sample, but at different excitation laser power. It can be seen in Fig. 3.3(a), no additional trapping that could increase the local concentration, can be observed. This indicates that the average number of particles $\langle N \rangle$ in the effective volume remains constant as the excitation laser power changes (shown in Fig. 3.3(b)).

Next, I calibrated the average particle number in the observation volume. Polystyrene nanospheres with radius 110 nm and 48 nm labeled with Firefli fluorescent red dye were serially diluted across three decades in concentration (from 100 nM to 100 pM). Assuming that the measured signal fluctuations are only caused by particle diffusion in and out of the FCS focal volume, which is true for diluted suspensions used here, the initial amplitude of the autocorrelation function $G(0)$ must be equal to the inverse number of fluorescent molecules in the effective volume. When the

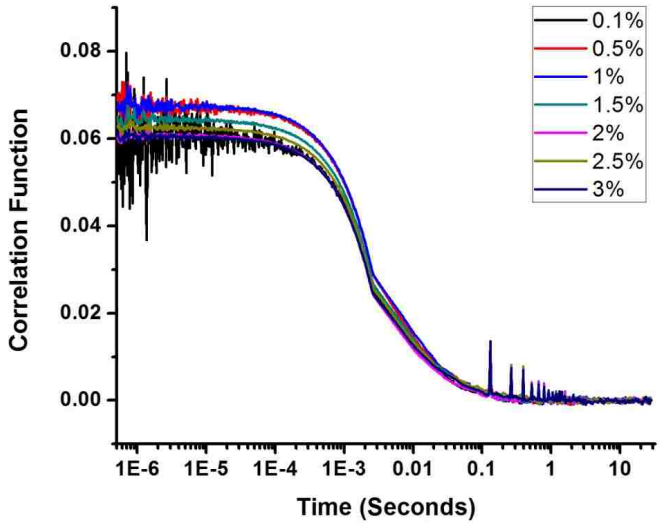

(a) Correlation functions obtained using the same sample, but with different excitation laser powers.

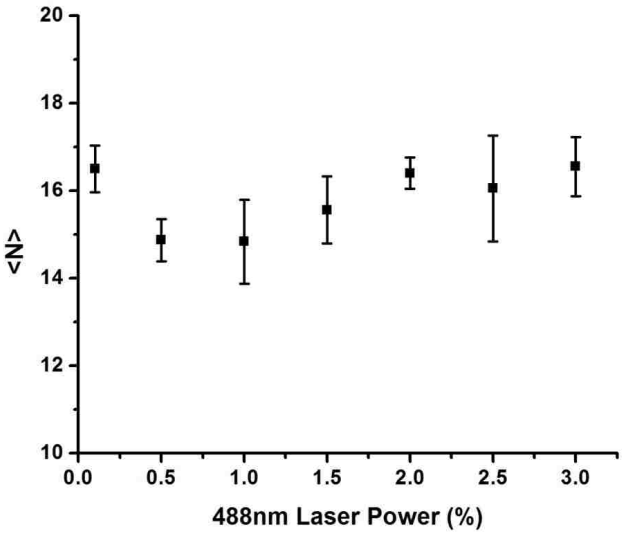

(b) $\langle N \rangle$ remains constant when changing the excitation laser power

Figure 3.3: The dependence of the correlation functions on the power of the excitation light.

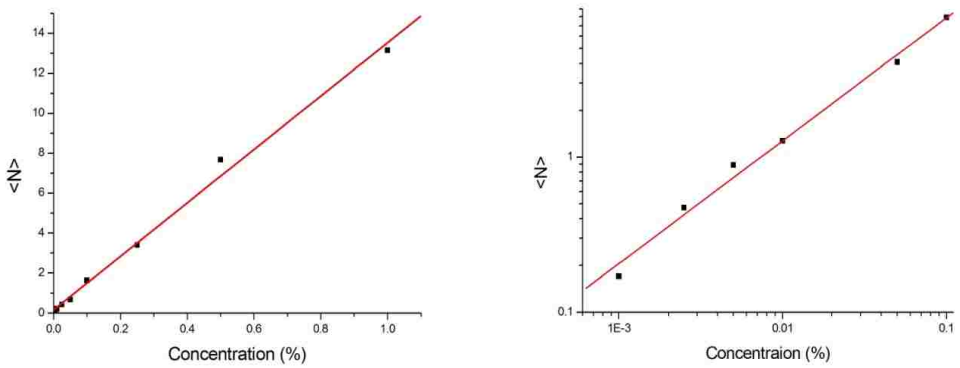

(a) 110 nm particles

(b) 48 nm particles

Figure 3.4: The linear relationship between the average number of particles in the effective volume and the known concentration of the particle suspension.

particle number in the effective volume is plotted as a function of the bulk concentration (Fig. 3.4), a linear relationship is observed, as expected. This demonstrates that our system is well calibrated for determination of the mean particle number.

3.3.2 Determination of the effective observation volume

As shown above, FCS directly measures the number of nanoparticles in the focal volume through the amplitude of autocorrelation function. To convert this information into an actual value of the particle concentration, the effective focal volume has to be experimentally determined. Two methods are commonly used to determine the effective volume.

Determination of the geometrical parameters via FCS performed on known dye molecules

The most common method for measuring the geometrical parameters (such as beam waist and shaping factor) is by measuring the correlation function of Alexa 488 molecules with known diffusiion coefficient ($D = 435\mu m^2/s$ at $22.5°C$)). Alexa 488 is diluted in deionized water to a concentration of 10 nM. By fitting the correlation curve obtained from molecules with known diffusivity, we determine the beam waist w_0 to be $0.25\mu m$, and the shaping factor S is 10.

Therefore, the effective volume is

$$V_{eff} = \pi^{3/2} w^3 S = \pi^{3/2} \cdot 0.25\,\mu m^3 \cdot 10 = 0.87 fL \tag{3.1}$$

Average number of particles as a function of known concentrations

In this approach, we plot the particle number in the observation volume as a function of a known concentration, (shown in Fig. 3.5). Because $C = N/V$, the observation volume can be found from the slope of the linear fit of the average number of particles versus known concentration:

$$V_{eff} = Slope = 8.84 \times 10^{-13}(mL) = 0.88 fL \tag{3.2}$$

Taking an average of the values given by the two methods, the effective observation volume is determined to be $0.88 \pm 0.01 fL$.

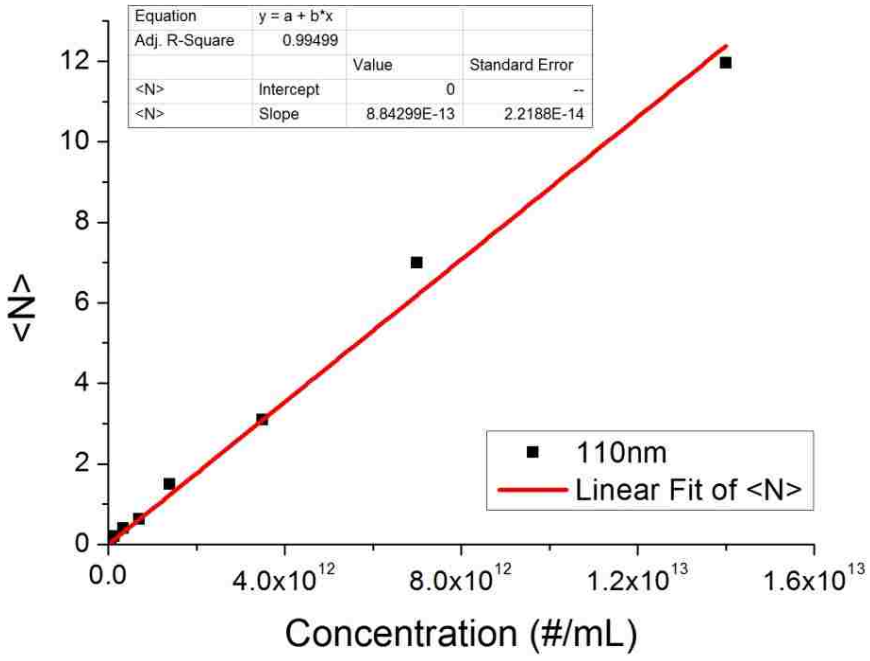

Figure 3.5: Linear dependence between an average number of particles and known concentrations.

3.3.3 Calibration of the diffusion coefficient

To confirm the values of the diffusion coefficient obtained from the FCS measurement, we compare it to the results given by the dynamic light scattering (DLS). DLS is a mature technique widely used to determine the size distribution of small particles in suspensions. According to the Stokes-Einstein relation (Eq. 3.3), radii of particles can be calculated from the diffusion coefficient. In this experiment, polystyrene nanoparticles of six different radii ranging from 20 nm to 200 nm are measured simultaneously by FCS and DLS. As observed in Fig. 3.6, the techniques yield similar radius values for particles with radii up to 60 nm, however they slightly disagreed for particles with radii above 80 nm.

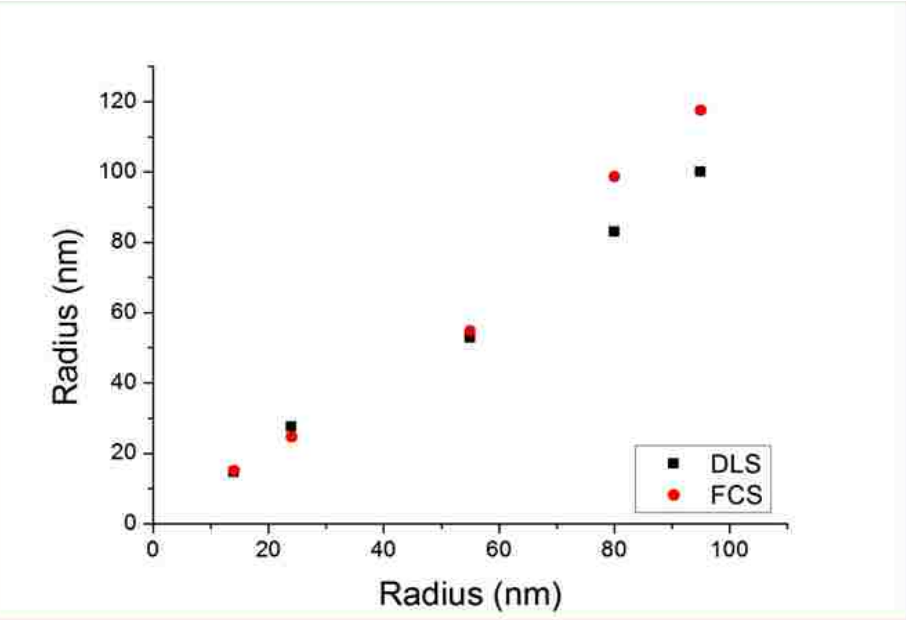

Figure 3.6: Comparison of the radii values obtained by FCS and DLS. The values on the horizontal axis are those specified by the manufacturer.

$$D = \frac{k_B T}{6\pi\eta R_h} \Rightarrow R_h = \frac{k_B T}{6\pi\eta D} \tag{3.3}$$

3.3.4 Corrections to the standard FCS correlation function

The derivation of the FCS autocorrelation function (Section 2.2.4) is based on the assumption that particles are significantly smaller compare to the wavelength of light, and thus can be treated as point fluorescent sources. However, experimentally, the size of particles cannot be neglected, especially for particles with sizes comparable to the dimensions of the observation volume. Appropriate corrections

to the autocorrelation function are included in the following equations [12].

$$G(\tau) = \frac{1}{N_A}\left(1+\frac{\tau}{\tau_A}\right)^{-1}\left(1+\frac{\tau}{\tau_d \cdot S_A^2}\right)^{-1/2} \tag{3.4}$$

In the above equation, the parameters N_A, S_A and τ_A, represent the apparent number of particles, apparent shaping factor, and apparent diffusion time respectively, which are related to the size of the particles as follow:

$$N_A = N(1+8a^2/5)\sqrt{1+8a^2/5S} \tag{3.5}$$

$$\tau_A = \tau_D(1+8a^2/5) \tag{3.6}$$

$$S_A = S\sqrt{(1+8a^2/5S)/(1+8a^2/5)} \tag{3.7}$$

where $a = \frac{A}{w_0}$ is the ratio of the diameter of particles to the beam waist.

From the equations above, the experimentally measured residence time, the number of particles in the volume, and the volume all appear to be larger than their actual values. After I corrected the data shown in Fig. 3.6 according to Eq. 3.5, the corrected data is shown in Fig. 3.4. By comparing the graph without (Fig. 3.7 left) and with (Fig. 3.7 right) the size-effect correction, it is clear that the corrected values are in better agreement with the linear relationship. This indicates that the size of the particles must be taken into account for the analysis of the autocorrelation function.

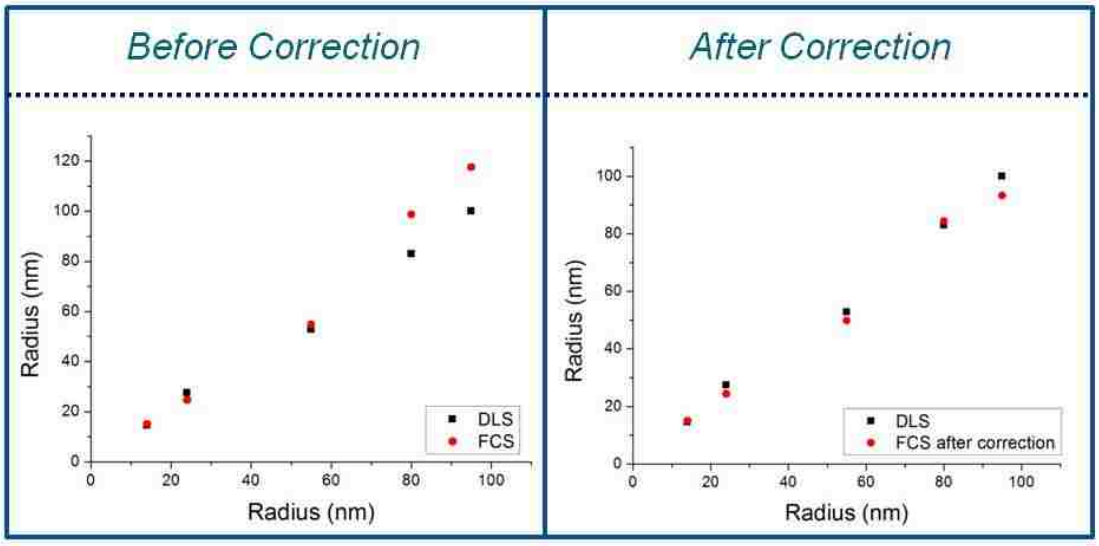

Figure 3.7: Correction of FCS due to particle finite size. (Left) result obtained from the standard autocorrelation function. (Right) data corrected using the size-corrected autocorrelation function.

3.4 Experimental results and discussion

To study the effect of trapping on the FCS autocorrelation function, I utilized two independent laser beams: a trapping beam with tunable power, and an excitation beam at a fixed power. The setup is shown in Fig. 3.1. In this experiment, to find the relationship between the amplitude of correlation function and the trapping energy, I perform FCS measurements from the 110 nm colloid nanoparticle suspension at trapping laser powers ranging from 0 to 16 mW. The resulting autocorrelation curves are shown in Fig. 3.8, where each curve represents an average of 10 independent measurements at the same trapping power. Using Eq. 2.22 to fit the trap-free curve yield $\langle N_0 \rangle = 0.165$ (average number of particles in the observation volume) and $D = 4.5\ \mu m^2/s$, where $\langle N_0 \rangle$ corresponds $\langle N \rangle$ at zero laser power. This value of

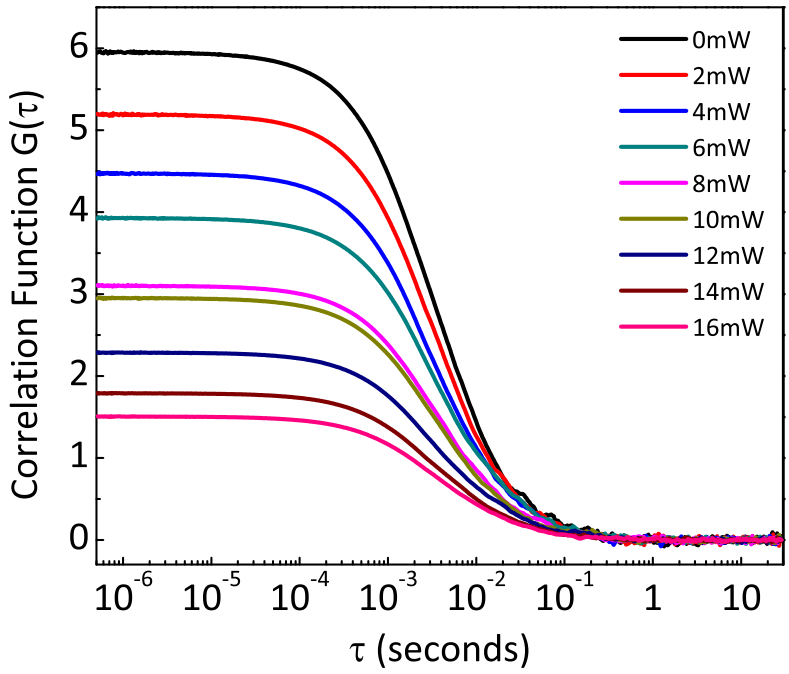

Figure 3.8: FCS autocorrelation functions of 0.01% (v/v) nanoparticle suspensions in different trapping laser powers. Each curve represents an average of 10 measurements

D agrees with the Stokes-Einstein value $D = k_B T/(6\pi\eta a) = 4.35\ \mu m^2/s$, where η is the viscosity of DI water at the ambient concentration and a is the particle radius. Comparison of $\langle N_0 \rangle$ with the known particle concentration indicates that corrections to Eq. 2.22 due to finite particle size are negligible [35].

Next, I intend to find out the relationship between $G(0)^{-1}$ and the average number of particles in the observation volume for the system in a potential well. First, the average brightness of each particle ϵ is determined by the ratio of $\langle F \rangle$ and $\langle N_0 \rangle$ at zero trapping power. Therefore, the average number of particles in the trap $\langle N_F \rangle$ can be calculated from the average photon counts $\langle F \rangle$ divided by ϵ. Fig. 3.9 shows a plot of $G(0)^{-1}$ (obtained from Fig. 3.8) vs. $\langle N_F \rangle$. The dashed line has

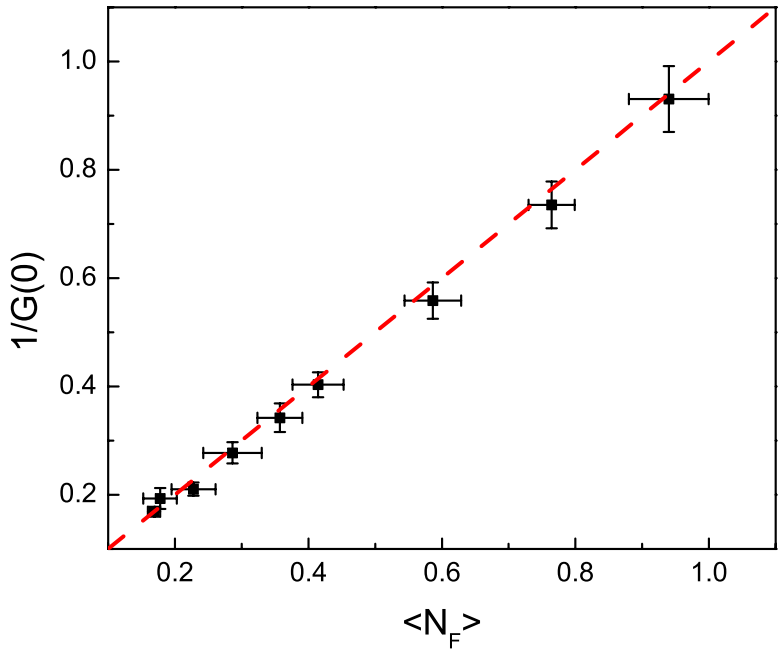

Figure 3.9: $G(0)^{-1}$ increases linearly with $\langle N_F \rangle$ measured by the average fluorescence photon counts normalized by the average brightness of each particle. For reference, the dashed line has slope 1 and intercept 0. The error bars are standard deviations for 10 repetitions of each measurement.

slope of 1 and goes through the origin. The linearity of the graph validates Eq. 2.23 for dilute sub-micron particles in an optical potential. Hence, the particle number density in the middle of the trap $\langle N_{trap} \rangle$ can be obtained from the inverse of the ACF amplitude.

For convenience, I define P the ratio of $G(0)^{-1}$ and $\langle N_F \rangle$:

$$P = \frac{G\left(0\right)^{-1}}{\langle N \rangle} = \frac{\langle N \rangle^2 / \langle \Delta N^2 \rangle}{\langle N \rangle} = \frac{\langle N \rangle}{\langle \Delta N^2 \rangle} \tag{3.8}$$

where $\langle \Delta N^2 \rangle$ is the variance of the particles. For systems that follow a Poisson distribution, $Var\,(N) = (\Delta N)^2$, therefore $P = 1$. In the experiment described earlier, we found that indeed $P = 1$, so the number of particles in the observation volume can be described by a Poisson distribution. Anyhow, the limitation of the Poisson distribution will be demonstrated later.

From the experiment above, the particle number density $\langle N \rangle$ in the trap can be obtained from G(0) of the ACF curves. In Fig. 3.10 we plot $\langle \mathrm{N_{trap}} \rangle / \langle \mathrm{N_0} \rangle$ vs. the laser trapping power P on a semi-log graph. The optical radiation pressure caused by the focused laser beam and the osmotic pressure produced by the enriched particle concentration in the trap are at equilibrium [11, 36]. The number of particles in optical confinement increases with the trapping laser power, following the Boltzmann distribution:

$$G\,(0)^{-1}_{trap} = \langle N_{trap} \rangle = \langle N_0 \rangle \exp\left(\frac{U_{trap}}{k_B T}\right) \tag{3.9}$$

where U_{trap} is the depth of the trapping potential, N_{trap} is the number of particles in the observation volume which is embedded in the optical trap. Such behavior corresponds to an ideal-gas-like cituation where particle interactions are negligible. This result is consistent with the fact that, at the low concentrations used here, the particle-to-particle distance ($\sim 2\,\mu m$) is much greater than the Debye screening length ($\sim 30\,nm$). The trapping energy of 100 nm polystyrene spheres used in this experiment, determined through the exponential fit in Fig. 3.10, is $0.1 \pm 0.04\,k_B T$ for each mW of laser power. This result shows a good agreement with the trapping energy reported elsewhere [11, 37].

Next, we plotted the ratio of $G(0)^{-1}$ and $\langle N_F \rangle$ obtained from Fig. 3.9 versus the trapping energies at different laser power. The ratio P equals to 1 for trapping

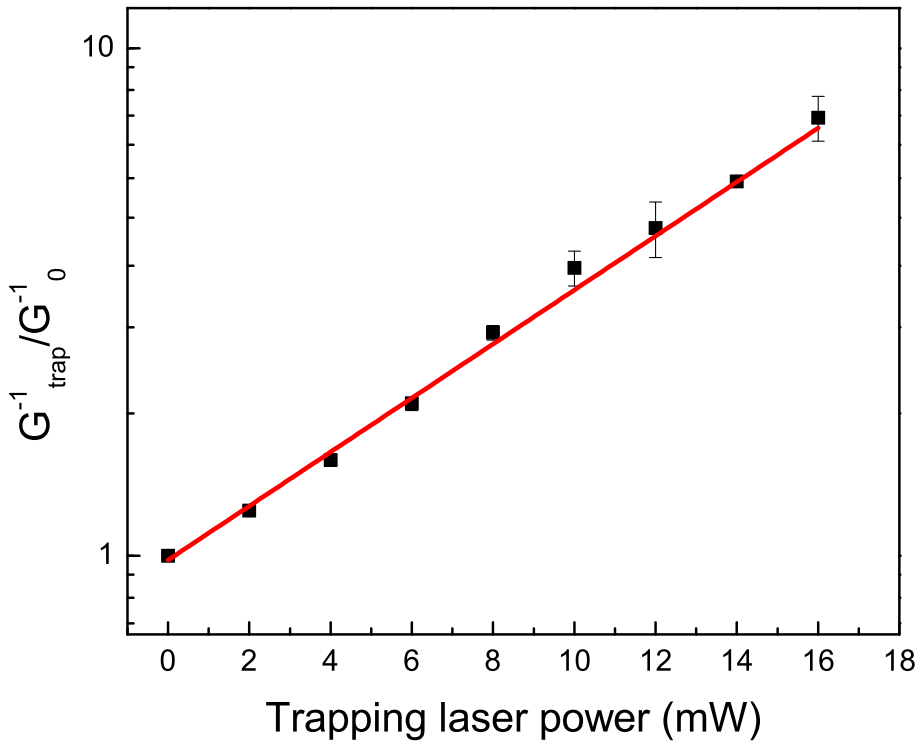

Figure 3.10: The enhancement of number of particle in the observation volume versus the trapping laser power. The error bars are obtained from 10 measurements at the same laser power. The linear appearance confirms the Boltzmann distribution of particles in the trap.

energies as large as 2 k_BT, shown in Fig. 3.11. This result verifies the theoretical prediction by Meng et al. [26].

From the statistical point of view, the ACF amplitude $G(0)$ is the ratio of the variance and the square of mean number of particles present in the observation volume. The probability of finding a particular particle in the trap can be estimated by multiplying the trap-free probability by a Boltzmann factor $exp(U_{trap}/k_BT)$. In

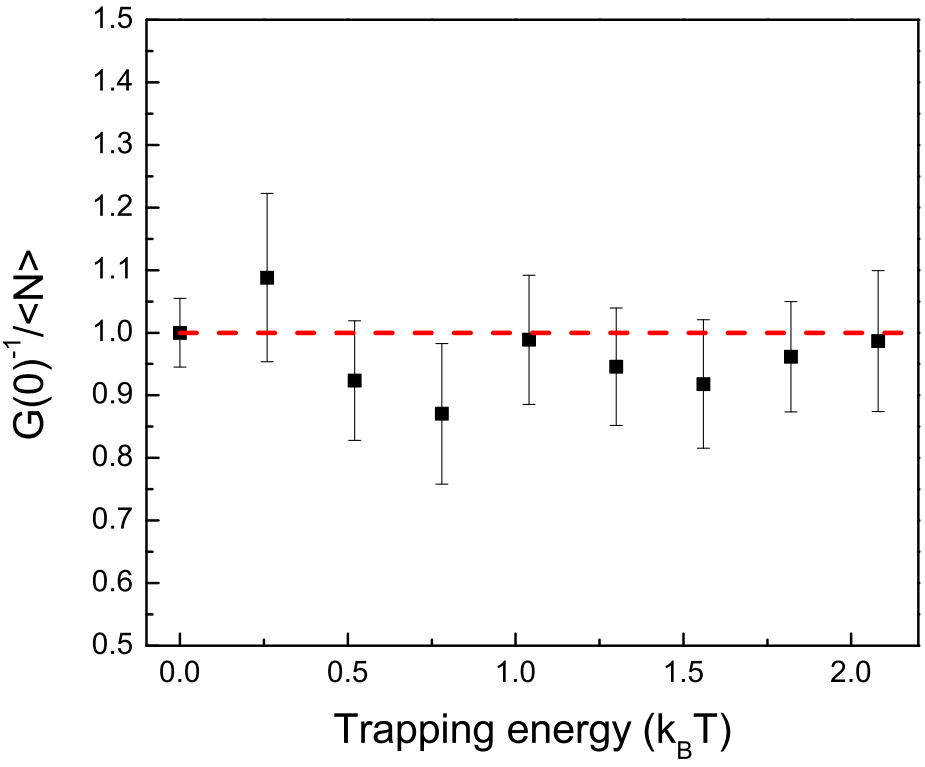

Figure 3.11: $G(0)^{-1}$ equals $\langle N \rangle$ for trapping energies less than 2 $k_B T$. For convenience, the dashed line gives $P = 1$.

the absence of an optical potential well, this probability is simply the ratio of the detection volume to the sample volume. The former is the volume of the laser focus (on the order of one femtoliter), while the latter is on the order of ten microliters. Thus, the probability for a particular particle to enter the FCS observation volume in the zero-trap condition is of the order of 10^{-10}. Since the Boltzmann factor is on the order of 10 in our experiment, the trapping-enhanced probability is still significantly less than one. Such a low probability ensures a Poisson distribution of probability of finding a particle in the trap, which satisfies the premises for Eq. 2.23.

We anticipate that when particles are tightly trapped with high trapping energies on the order of 10 k_BT and higher, the Poisson approximation would become invalid as discussed next.

Chapter 4

Fluorescence correlation spectroscopy of interacting colloidal nanoparticles in an optical trap

In the previous Chapter, we discussed the statistics of nearly ideal system in an optical trap. However, particle interactions can hardly be avoided in reality. For many-body systems made up of a large number of interacting particles, both the dynamics and statistics of nanoparticles in suspension would be affected. In this Chapter, I will first show experimentally how Coulomb interaction between the double layers of the particle surfaces bias the initial amplitude of FCS autocorrelation function. I will generalize a theory of FCS to describe non-ideal systems of

interacting particles. The behavior of interacting nanoparticles under a trapping potential will also be discussed.

4.1 Experimental characterization of particle interaction

In this section, I experimentally measure P, the ratio between $G(0)^{-1}$ and $\langle N \rangle$, and study its dependence to the Coulombic forces. A serial dilution from concentrated suspensions of 160 nm particles at volume fractions about 15% in deionized water and a serial dilution of the same particles in 50 mM potassium chloride solution are prepared for this experiment. The initial amplitude $G(0)$ is determined from the FCS correlation function. The mean particle number $\langle N \rangle$ is measured from the photocount divided by the average brightness of each particle. I plot P versus the average distance between the surface of nearby particles (Shown in Fig. 4.1). The x-axis indicates the average distance between the surfaces of two nearby particles D_{s-s} calculated from:

$$D_{s-s} = \left(\frac{V_{obs}}{\langle N_F \rangle} \right)^{1/3} - D_{160} \tag{4.1}$$

where V_{obs} is the observation volume and D_{160} is the diameter of the particle.

The result indicates that for particles in deionized water, P (Eq. 3.8) deviates significantly from 1 when the average distance between the surfaces of nearby particles is below 300 nm; while for particles in a salty medium with 50 mM KCl, P remains constant for D_{s-s} as close as 100 nm.

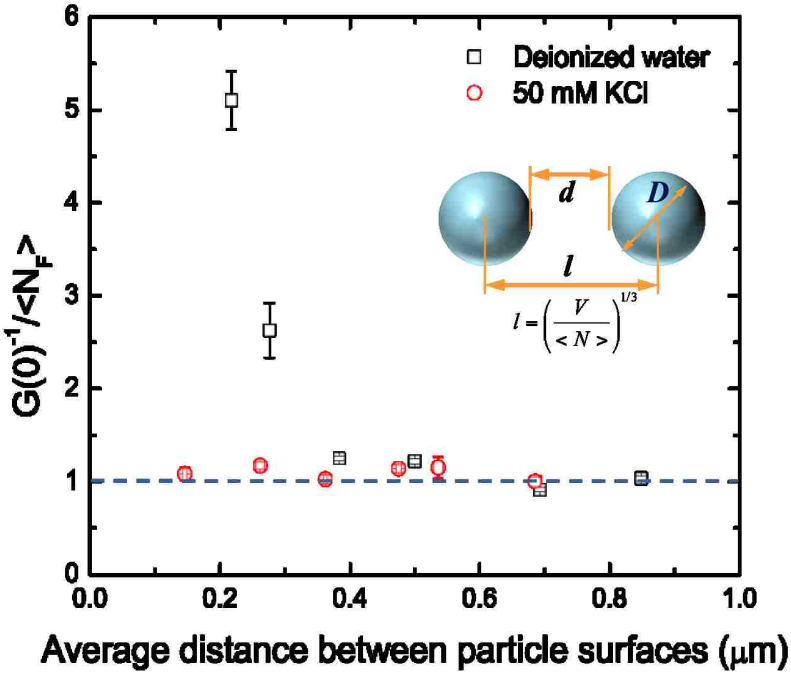

Figure 4.1: The ratio of $G(0)^{-1}$ and $\langle N_F \rangle$ is plotted versus the average distance between the surfaces of two nearby particles. A dilution series of concentrated suspensions of 160 nm particles are prepared both in deionized water (black squares) and 50 mM potassium chloride (red circles). Both the initial amplitude $G(0)$ and the average number determined by the fluorescent photon counts are measured.

I calculated the Debye length that characterise the length of the interfacial electrical double layer (EDL) on the particles in the two different solutions using the following equation,

$$\lambda_D = \frac{1}{\sqrt{8\pi\lambda_B N_A I}} \tag{4.2}$$

where λ_B is the Bjerrum length of the medium, which is about 0.7 nm for water, I is the ionic strength of the medium. For particles in deionized water, the ionic strength is estimated to be 5 μM, thus the Debye length is 140 nm. For particles in 50 mM KCl solution, the Debye length is 1.4 nm.

The Deyaguin-Landau-Verwey-Overbeek (DLVO theory) that describes the force between charged surfaces interacting through a liquid medium, combines the effects of the van der Waals attraction and the electrostatic repulsion due to the EDL.

The van der Waals interaction energy between two identical spheres with radius R can be calculated as:

$$U(D) = -\pi^2 \rho^2 \frac{R}{2D} \tag{4.3}$$

where ρ is the number density of the particle in the solution.

For long range interaction ($D = 300\,nm$ in this experiment), the van der Waals interaction is weak. The Coulomb interaction between the EDL of nearby spheres is dominant. The interaction energy between two spheres of radius R can be written as

$$U = \left(64\pi k_B T R \rho_\infty \gamma^2 \lambda_D^2\right) e^{-D/\lambda_D} \tag{4.4}$$

where ρ_∞ is the number density of ion in the bulk solution and γ is the surface potential.

For particles with radius $R = 80\,nm$, debye length $\lambda_D = 140\,nm$, surface potential is estimated to be $\gamma = 100\,mV$, in the solution with number density of ions $\rho_\infty = 3 \times 10^{18}/L$, and separated by an average distance $D = 300\,nm$, the interaction free energy is calculated to be 1.6 $k_B T$. In real colloidal particle system, besides the two-body interaction, many-particle interaction also exists. Therefore, we anticipate that the actual interaction energy would be higher than $1.6\,k_B T$. Overall, when interaction free energy is much higher than the thermal energy of the particles ($1.5\,k_B T$), the bias due to the Coulombic force to the FCS autocorrelation function cannot be neglected.

4.2 Ensemble theory of FCS in non-ideal system

In this section, I will generalize a theory for the inital amplitude of FCS correlation function for interacting particle suspension.

We have discussed in Chapter 2 that the initial amplitude of FCS correlation function can be given as:

$$G(0) = \frac{\langle N^2 \rangle - \langle N \rangle^2}{\langle N \rangle^2} \tag{4.5}$$

For a one-species system, the grand canonical partition function is given by

$$\Xi(V, T, \mu) = \sum_N Q(N, V, T)\, e^{-\mu N / k_B T} \tag{4.6}$$

where Q is the canonical partition function, V is the volume of the system, T is the temperature, and μ is the chemical potential.

Thus, we can write:

$$\langle N^2 \rangle = \frac{1}{\Xi} \sum_N N^2 Q(N, V, T)\, e^{-\mu N / k_B T} \tag{4.7}$$

It can be shown that

$$\langle N^2 \rangle = \langle N \rangle^2 \frac{k_B T \kappa}{V} + \langle N \rangle^2 \tag{4.8}$$

where κ is the isothermal compressibility. Therefore, Eq. 4.5 can be rewritten as [38]:

$$G(0) = \frac{k_B T \kappa}{V} \tag{4.9}$$

The compressibility κ is defined as the relative volume change of a fluid as a response to a pressure change

$$\kappa = -\frac{1}{V}\frac{\partial V}{\partial P} \tag{4.10}$$

where V is volume and P is pressure.

For an ideal gas system, which has the equation of state $PV = Nk_BT$, the compressibility is $\kappa = \frac{V}{Nk_BT}$. The initial amplitude of the FCS autocorrelation function Eq. 4.9 can be simplified to the familiar expression

$$G(0) = \frac{1}{N} \tag{4.11}$$

For a non-ideal system, such as a many-particle system where particle interaction cannot be neglected, the compressibility can be expanded by a virial expression:

$$\kappa = \frac{V}{k_BT}\left(1 + 2B_2N + 3B_3N^2 + ...\right)^{-1} \tag{4.12}$$

where B_i are the virial coefficients, characterizing the interaction potential between the particles. The second virial coefficient B_2 depends only on the pair interaction between particles, the third virial coefficient B_3 depends on 2-body and non-additive 3-body interactions, and so on.

Therefore, the amplitude of autocorrelation function (ACF) is derived in the following form:

$$G(0)^{-1} = \langle N \rangle \left(1 + 2B_2N + 3B_3N^2 + ...\right) \tag{4.13}$$

This generalized equation can be used to calculate the virual coefficients and

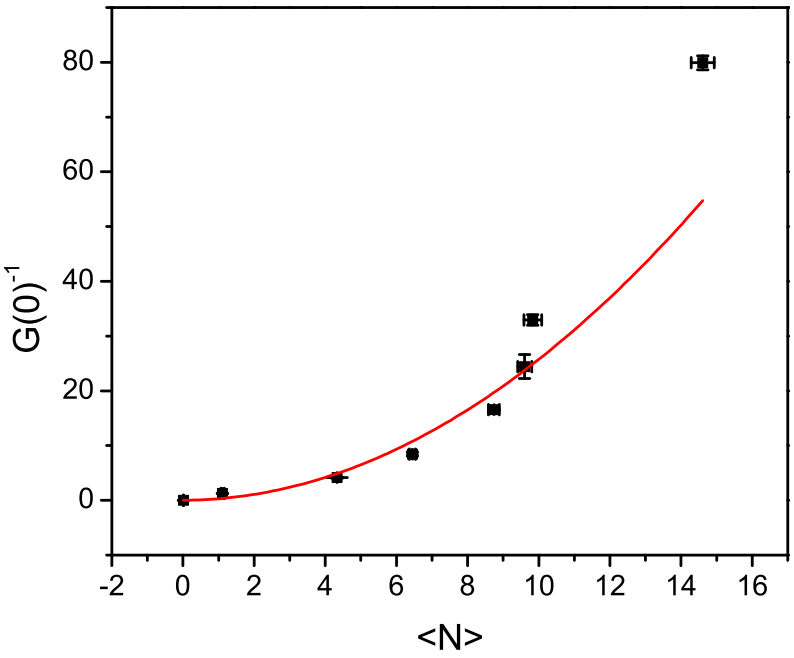

Figure 4.2: The ratio between $G(0)^{-1}$ and $\langle N \rangle$ versus the particle number in the detection volume. The virial coefficients can be determined via a polynomial fit.

thus characterize the interaction potential.

A serial dilution of particles with diameter 160 nm is prepared in deionized water for this experiment. The ratio between $G(0)^{-1}$ and $\langle N \rangle$ is plotted versus $\langle N \rangle$, as shown in Fig. 4.2. I fit the data with Eq. 4.13 to obtain the virial coefficients.

4.3 Interacting nanoparticles in an optical trapping potential

A focused laser beam confines nanoparticles and increases the particle concentration at the laser focus, thus both the particle-light and particle-particle interactions

need to be considered. Therefore, P, the ratio between $G(0)^{-1}$ and $\langle N \rangle$, can reflect the effect of two factors that causing the breakdown of Poisson statistics of the nanoparticles in suspension. One factor is the particle interaction caused by enhanced local concentration that we discussed in the previous sections, and the other is the trapping-enhanced probability for a particular particle to the present in the optical trap.

To study how optical forces bias the initial amplitude of FCS correlaton function, I focused a trapping laser on diluted suspensions of 160 nm particles at a constant volume fraction of 0.08%, but prepared in either de-ionized water or 50 mM KCl solution. The FCS measurements were carried out in the center of the trapping laser focus. As shown in Fig. 4.3, the ratio P deviates from unity at a trapping energy of $2\,k_BT$ for particles in de-ionized water, while in contrast, to the high salt condition ($50\,mM$ KCl), the relation $G\,(0) = 1/\langle N \rangle$ is valid for trapping energies lower than $6\,k_BT$.

To find out whether the breakdown of Poisson statistics is caused by particle-light or particle-particle interaction, I compared the above result with Fig. 4.1 where only interparticle interaction is considered. Fig. 4.4 shows the ratio P plotted against the average distance between the surfaces of two nearby particles in (a) deionized water and (b) $50\,mM$ KCl solution. The number density of the particles in the observation volume is controlled either by serial dilution (solid squares in Fig. 4.1) or by changing the trapping laser power (empty squares). Comparing the two sets of data both obtained in deionized water, P deviates from unity when $D_{s-s} < 0.35\mu m$, when the double layers of the two nearby particles overlap. Therefore, the bias of $G(0)$ is caused by particle interaction due to Columbic forces. For Fig. 4.4(b),

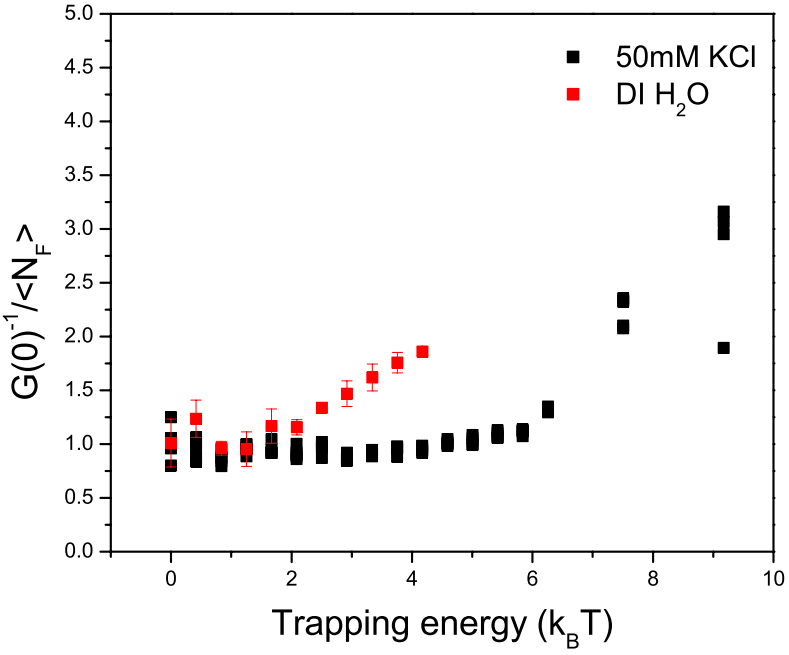

Figure 4.3: The ratio P is plotted versus the trapping energy of 160 nm particles in an optical confinement. Samples are prepared at the same volume fraction of 0.08%, either in 50 mM KCl solution (black squares) or deionized water (red squares) respectively. The range where $P = 1$ is significantly extended in a salty medium, in which particle interaction is significantly dampened.

comparing the two sets of data both obtained in $50\,mM$ KCl solution, P was found to significantly deviate from unity at $D_{s-s} < 0.3\mu m$ for particles under optical forces, while P remains 1 for particles in serial dilutions. The double layer of the particles in $50\,mM$ KCl solution is $1.4\,nm$, thus the Coulomb interaction energy is very low for particles seperated by $0.3\,\mu m$. The bias of $G(0)$ away from $1/N$ is therefore caused by the trapping potential due to optical trapping forces. Thus, $6\,k_BT$ sets a practical limit of $G\,(0) = 1/\langle N \rangle$ for non-interacting particles inside an optical trap.

4.4 Conclusions

In this Chapter, I found that particle interaction caused by the Coulomb forces between the electric double layers on the particle surfaces bias the Poisson statistics when interaction energy is much larger than the thermal energy of the system. Based on the bias of the relation $G(0) = 1/\langle N \rangle$, A generalized theory of FCS describing non-ideal system consists of interacting particles was derived. This theory can be used to obtained the virial coefficients, and the compressibility of interacting colloidal particles. Optical trapping applies forces on the particles near the laser focus and increases particle concentration thus increase particle-particle interaction. Both Coulomb interaction energy and optical trapping energy can cause a bias to the particle statistics in an optical trap. I experimentally determined that the nanoparticles in an optical potential with trapping energies higher than $6\,k_B T$ would have a significant effect on the Poisson statistics. It should also be noted that by changing the particle density we have also increased the hydrodynamic interactions between the particles causing correlated movement of one particle with a nearby one. The effect of hydrodynamic interaction to number density fluctuation needs further exploration.

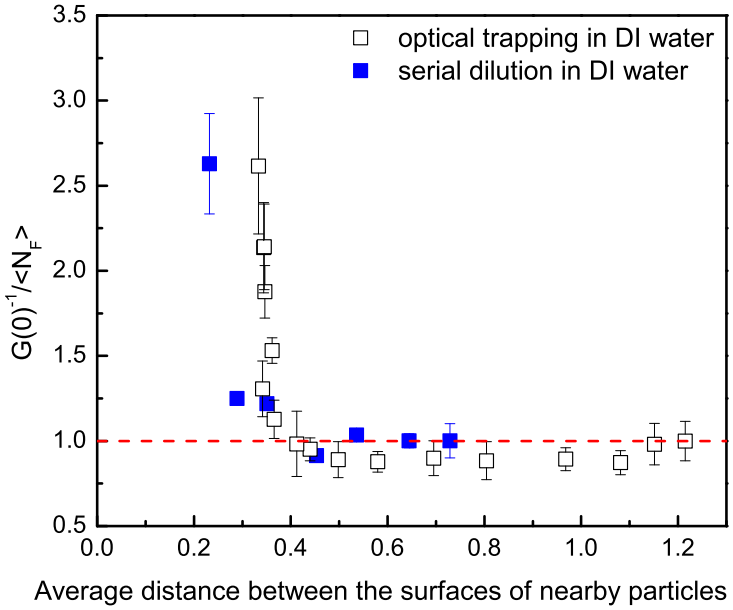

(a) Comparison of the Coulomb interaction and the optical trapping on the effect to Poisson statistics for particles in deionized water

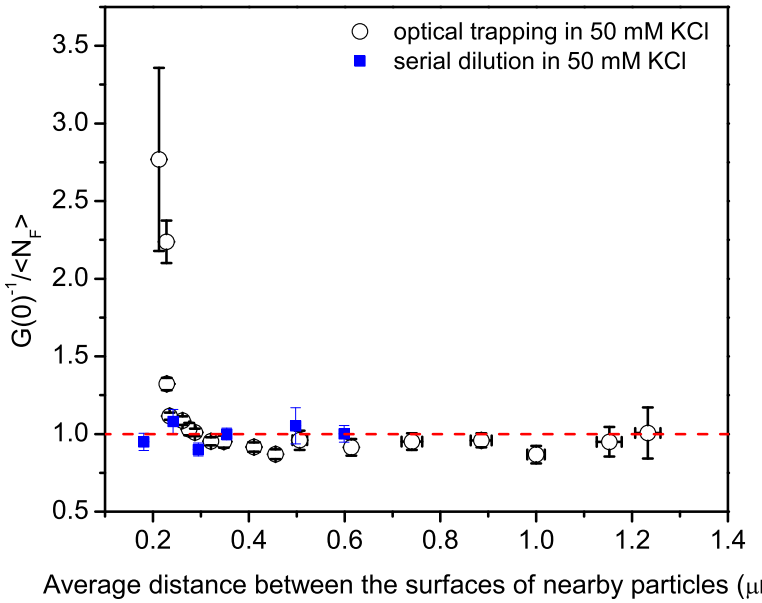

(b) Comparison of the Coulomb interaction and the optical trapping on the effect to Poisson statistics for particles in salty medium with 50 mM potassium chloride

Figure 4.4: This figure shows a comparison of the Coulomb interaction and the optical trapping on the effect to Poisson statistics. The ratio P is plotted versus the average distance between the surfaces of two nearby particles.

Chapter 5

Enumeration of HIV-1 virus-like particles (VLPs) in an optical trap by FCS

Concentration and quantification of dilute viral particle suspensions are essential for early diagnosis of many diseases such as AIDS. Recent reports show the possibilities of using dielectrophoresis or optical trapping methods to concentrate viral particles [7–9].

Because of their small size, simple biology, and obligate intracellular life cycle, viruses present significant detection challenges. Since the 1940s, there have been three general approaches for detecting viruses: (1) analysis of the host organism's response to the virus, especially antibody serology; (2) detection of a virus' molecular fingerprints, including viral proteins and viral nucleic acids; and (3) direct sensing

of whole viral particles. Recent viral detection methods are mostly based on nucleic acid amplification. Although accurate and quantitative, the measurement of viral concentration using existing commercial systems is prohibitively expensive and much too technically demanding for resource-poor settings.

New methods are emerging that directly detect and enumerate intact viruses, based on recent advances in optics, microfabrication, and nanotechnology [39–41]. Compared to molecular detection, whole particle viral detection has significant advantages in simple sample preparation and fast sample-to-assay time, thus holding great promise to bring improvements to the speed, sensitivity, operability, and portability of viral diagnostics. Among optical detection methods, FCS is well established for measuring the concentration and diffusion behavior of molecules in real time and self-calibrated fashion.

In this Chapter, I employ the method discussed in previous chapters to detection of HIV-1 virus-like particles (VLPs). I optically enhance the concentration of the virus through optical trapping and measure the number density by FCS. I determine the trapping energy of the VLPs, thus providing guideline for future applications on virus trapping.

5.1 Preparation of pseudo-HIV virus

5.1.1 Amplification of the plasmids

Four genes are used in the construction of pseudo-HIV virus. Their roles are listed below:

1. Rev: regulator of virion expression, allows fragments of HIV mRNA that contain a Rev response element to be exported from the nucleus to the cytoplasm.

2. Env: serves to form the viral envelope glycoproteins by a viral protease.

3. JRFL: together with the Env gene, it serves to form the HIV-1 gp-120 protein.

4. Gag-GFP: forms the structure of the pseudo-virus and green fluorescent proteins within the viral capsid.

Note that, for the production of virus-like particles (VLPs), only Gag-GFP plasmid is needed.

A plasmid is a small circular piece of DNA that contains genetic information for the growth of bacteria. It was discovered in the 1960's, and is now commonly used to amplify a gene of interest. The gene of interest is inserted into the vector plasmid which contains resistance to an antibiotic (typically ampicillin), and then put into *E. coli* that are sensitive to ampicillin. The bacteria are then spread over an agar plate which contains ampicillin. The ampicillin serves as a filter because only bacteria that have acquired the plasmid which contains resistance to ampicillin can grow on the plate. Therefore, as long as we grow the bacteria in ampicillin, the plasmid will be amplified as the growth of the bacteria.

After the cloning of the plasmids through bacteria, we used OriGene PowerPrep HP Maxiprep Kits to purify the plasmids from the debris of cell membranes. A decent concentration of each plasmid are produced.

For the transformation of each 60 mm plate of confluent cells, the amount of each plasmid listed above needed is: $5\mu g$, $10\mu g$, $20\mu g$ and $3\mu g$ respectively.

5.1.2 Construction of pseudo-HIV virus

Viruses are constructed through the process of cell transfection, which is a combination of transfer of DNA and infection of cells by the isolated nucleic acid from a virus. The three requirements of competent cells are: (a) uptake of viral nucleic acid; (b) replication of viral molecules; and (c) assembly of virus and release. Fig. 5.1 show an image of Human Embryonic Kidney 293T 17 cells (ATCC No. CRL-11268) we used for transfection. The cells are cultured in Dulbecco's Modified Eagle's Medium (DMEM) with 10 % concentration of fetal bovine serum (FBS) at $37°C$. Cells at 60% confluency are used for the transfection. The resulting viral particles have the same capsid structure as wild-type HIV virion, but lack some of the viral genome to minimize its pathogenicity. Moreover, these particles are labeled by green fluorescent proteins (eGFP, excitation maximum at 488 nm and emission maximum at 509 nm).

5.1.3 Cell transfection

Here are three types of transfection that are commonly used:

Chemical-based transfection

One of the cheapest and most common methods uses calcium phosphate. HEPES-buffered solution containing phosphate ions is combined with a calcium chloride solution containing the DNA to be transfected. When the two solutions are mixed, a precipitate of the positive charged calcium and the negatively charged phosphate will form, binding the DNA to be transfected on its surface. The suspension of the

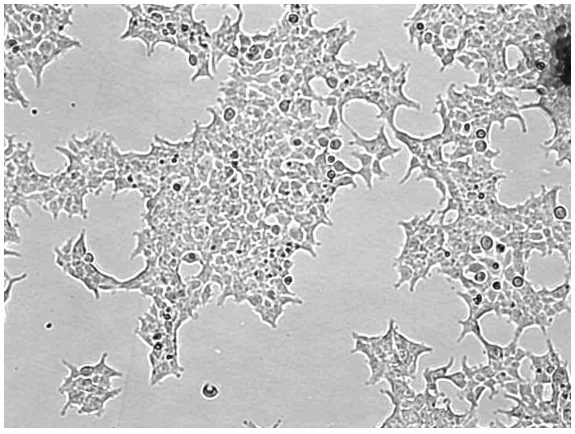

(a) image of HEK cells under 10× objective

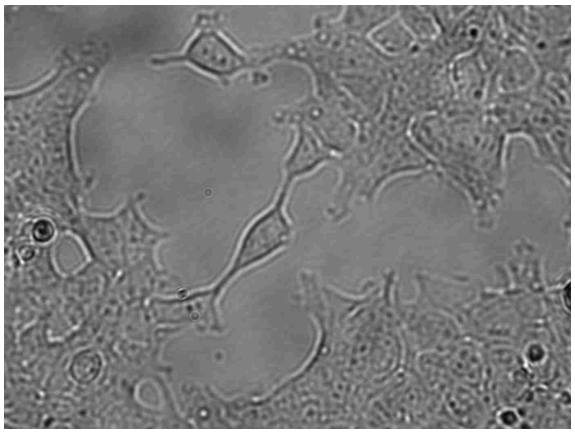

(b) Image of HEK cells under 40× objective

Figure 5.1: Microscope images of the HEK 293T 17 cells

precipitate is then added to the cells to be transfected. The DNA, together with the precipitate, is taken up by the cells.

Non-chemical transfection

A popular non-chemical method for transfection is *Electroporation*. By applying electric field to the cells, the electrical conductivity and permeability of the cell plasma membrane are increased. Thus, DNA can be up-taken by the cells. Other similar methods exist involving use of optical forces or hydrodynamic forces to open the cell membrane.

Particle-based transfection

A more direct approach for cell transfection is through the nanoparticles that have coupled with DNA. This method can deliver DNA directly into the nucleus of the target cells by manipulation of the nanoparticles.

5.1.4 Purification of the virus

The medium containing pseudo-virus was collected and filtered using $0.2\,\mu m$ filter and centrifuged for 3 hours at $20,000$ rpm with 20% sucrose layered beneath the medium. Because of the difference in the densities of sucrose, virus and debris of membrane, the virus is separated from the rest. Fig. 5.2 schematically shows the process of purification. Virus is collected from the centrifuge tube and re-suspended in cell culture medium.

5.1.5 Virus infectivity assay

One of the most commonly used laboratory methods for the detection of viruses and virus components in biological samples is virus infectivity. By adding the viruses

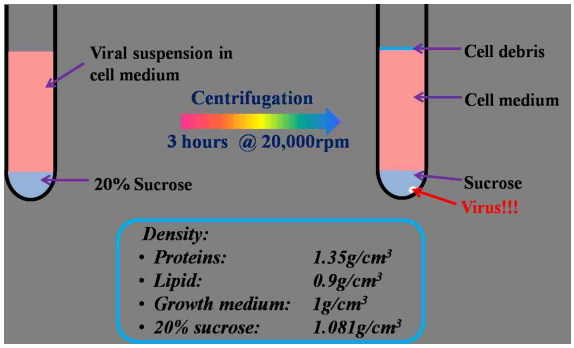

Figure 5.2: Virus purification

into cell suspension, cells will be infected. Here, we uses x-gal staining assay to test the infectivity of both the pseudo HIV viruses and the gag VLPs. We use TZM-bl cells, which stably expresses large amounts of CD4 and CCR5, and therefore highly sensitive to infection with HIV-1, for the infectivity assay. The cells are cultured in 96-well plates one day before the assay at $37°C$ with culture medium 90 % DMEM and 10 %FBS. The morphology of the cells is shown in Fig. 5.3. Mixing the virus with the TZMbl cells, $\beta - galactosidase$ gene is then induced for cells infected with HIV. X-gal, consists of an lactose, can be hydrolyzed by the $\beta - galactosidase$. When cleaved by $\beta - galactosidase$, X-gal yields galactose and 5-bromo-4-chloro-3-hydroxyindole, which will spontaneously dimerize and oxidize to $5, 5' - dibromo - 4, 4' - dichloro - indigo$ (insoluble blue product). Therefore, the blue-colored cells can be used as a test for infectivity of the viruses. Fig. 5.4 shows the results of the infectivity test for both the virus and the VLPs. A large amount of cells turned blue when infected by the pseudo-virus in Fig. 5.4(a), while no cells incubated with Gag VLPs are in blue color (Fig. 5.4(b)) meaning that the Gag VLPs are non-infectious.

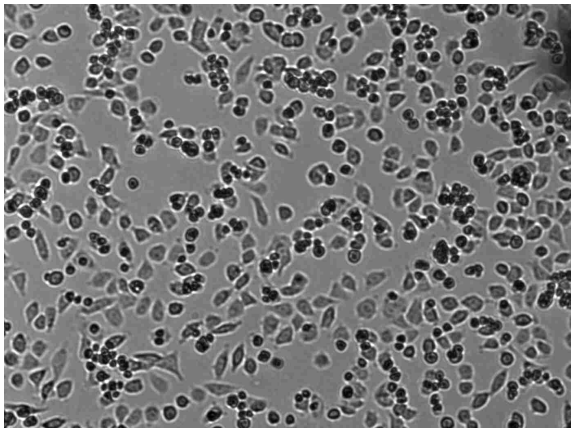

(a) image of TEM-bl cells under 10× objective

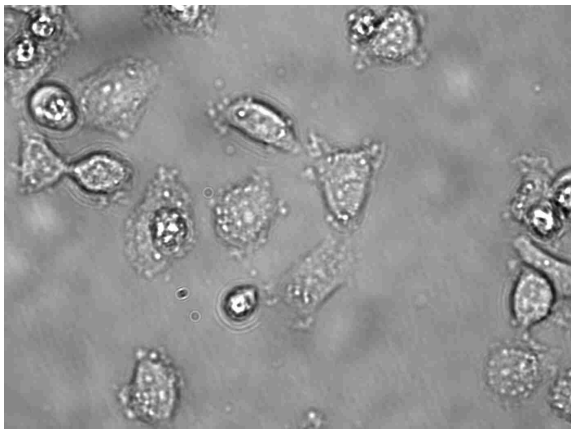

(b) Image of TZM-bl cells under 40× objective

Figure 5.3: The microscope images of the TZM-bl cells

5.1.6 Virus imaging

For SEM image of Pseudo HIV virus and VLPs on glass, we fixed the virus on a thin coverslip. We first added glutaraldehyde at a final concentration of 2.5% into the sample, and fixed at room temperature for 1 hour. A drop of the sample is then added on an autoclaved coverslip. Before the sample dries out, 50% ethanol was

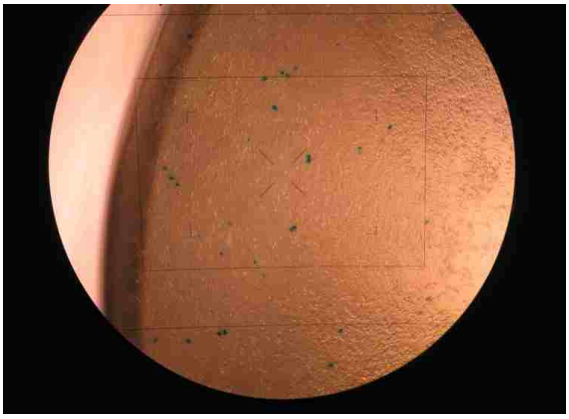

(a) Experimental result of the infectivity assay of the pseudo-HIV virus; the blue dots indicate that cells are infected.

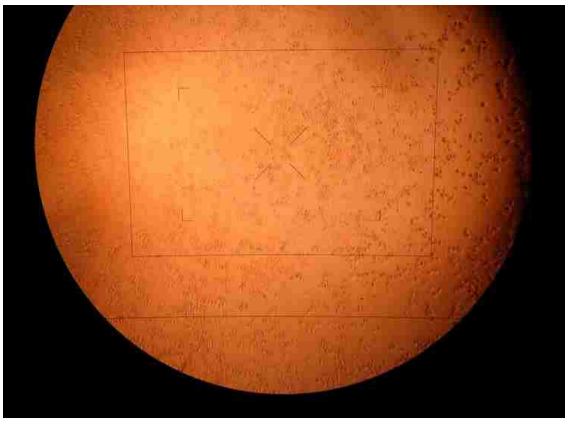

(b) Experimental result of the infectivity assay of the Gag VLPs; no blue dots are observed meaning that the VLPs are not infectious.

Figure 5.4: Infectivity assay

added on the coverslip for 10 min, then 75% ethanol for 20 min, 95% ethanol for 20 min and 100% ethanol for 20 min. SEM images are shown in Fig. 5.5.

A confocal image of the VLPs in buffer suspension is shown in Fig. 5.6.

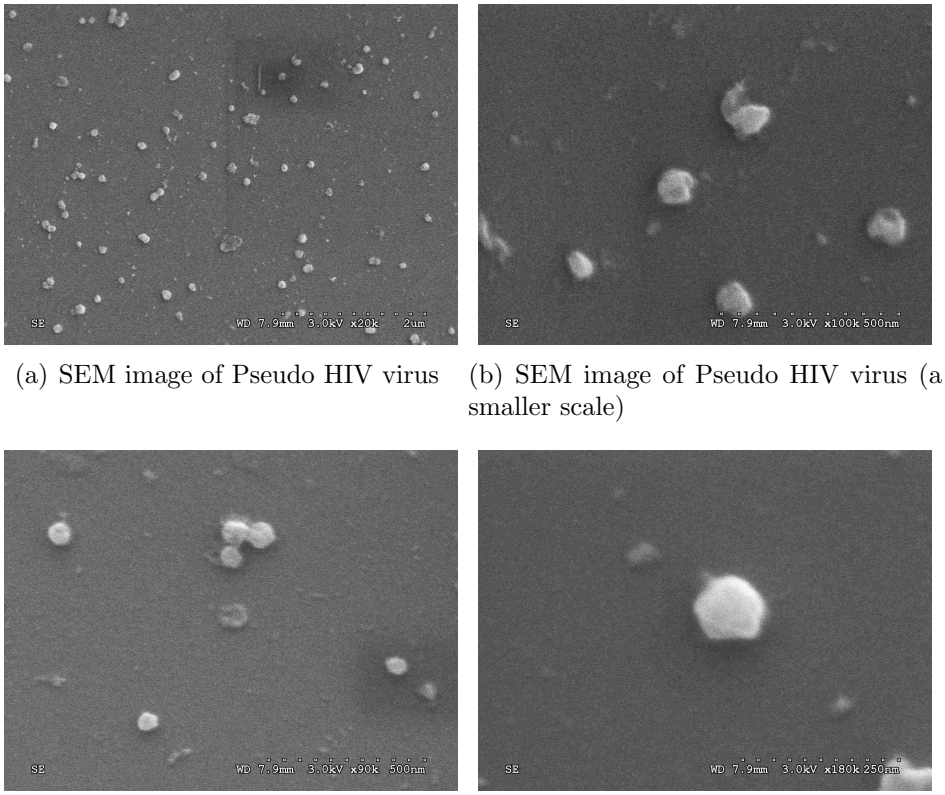

(a) SEM image of Pseudo HIV virus

(b) SEM image of Pseudo HIV virus (a smaller scale)

(c) SEM image of VLPs

(d) SEM image of VLPs (a smaller scale)

Figure 5.5: SEM images of the pseudo-viruses and the VLPs. The average sizes of both types of viral particles are around 120 nm in diameter.

5.2 Optical trapping of the virus

5.2.1 Experimental results

With the verification of Eq. 2.23 for sub-micron sized polystyrene spheres loosely confined in an optical trapping potential as we discussed in Chapter 3 and 4, I then applied this methodology on VLPs having a similar structure as the HIV virus. Fig. 5.5 shows the SEM images of the VLPs. The average diameter of the particles

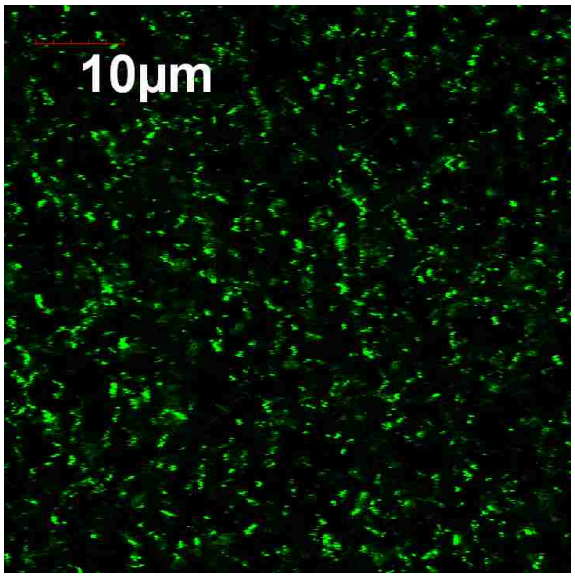

Figure 5.6: Fluorescence image of the VLPs in suspension.

is determined to be $110 \pm 11\,nm$, which agrees with previous studies [42, 43]. With an excitation laser wavelength of 488 nm, I took the fluorescent image of dried VLPs on a thin glass slide under 100× objective, shown in Fig. 5.6. I measured the FCS correlation functions of the VLPs suspended in culture medium. The diffusion coefficient is determined to be $3.79\,\mu m^2/s$ from the fitting curve using Eq. 2.22. The viscosity of the medium with main component DMEM is 0.98 cP at 20°C. The diameter of the VLPs calculated through the Einstein-Stokes equation $D = k_B T/6\pi\eta a$, is $115 \pm 14\,nm$ (average of 15 measurements), which is well agreed with the diameter determined through SEM images.

Next, we focused the external trapping laser on the viral suspension sealed between a microscope slide and a thin coverslip. The correlation functions at different trapping laser powers are obtained, selected curves are shown in Fig. 5.7 (a). The value $G(0)^{-1}$ of the curve is then plotted versus the operating trapping laser power

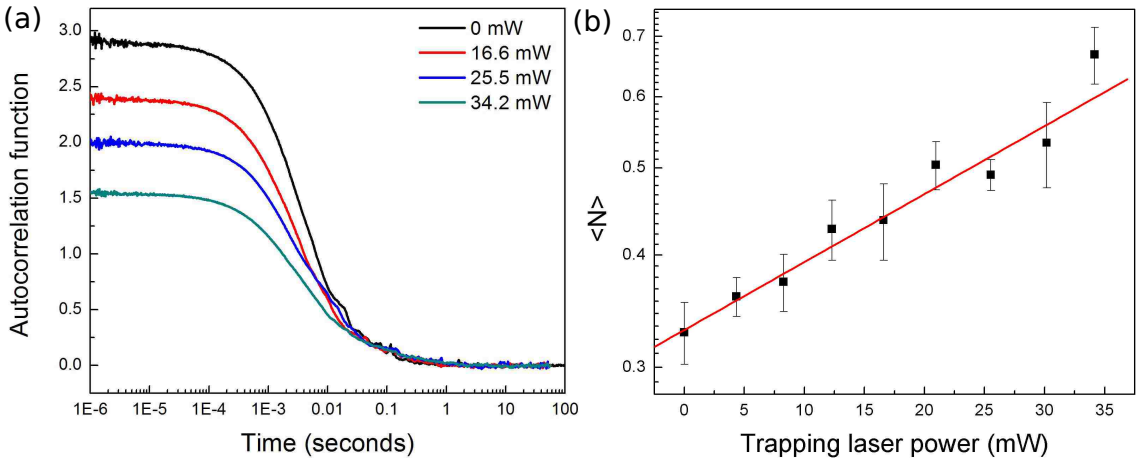

Figure 5.7: (a) Selected autocorrelation curves of VLPs in culture medium at different trapping laser powers. (b) The average number of particles in the observation volume versus the trapping laser power.

in semi-log scale, shown in Fig. 5.7(b). The fitting shows an exponential relation between the mean particle number and the trapping laser power. The trapping energy per VLP is thus determined to be $0.02\,k_BT$ for each mW of the trapping power. With higher trapping laser power, the concentration enhancement would increase exponentially. Knowing the VLP number density inside of the trapping laser allows us to determine the ambient number density.

The trapping energy for each VLP was measured to be $0.02\,k_BT/mW$. Compared with the single particle trapping energy for solid particle with the same diameter ($0.1\ k_BT$, discussed in Chapter 3), the trapping energy for VLPs is significantly smaller. However, the refractive index for polystyrene is 1.59, while for lipid it is about 1.46, thus significantly reducing the optical force on the particle. Next, I will theoretically simulate the trapping energy profiles of both vesicles and particle with the same diamter.

5.2.2 Theoretical simulations

Comparing the trapping energy of the VLPs with the solid polystyrene spheres we have measured in Chapter 4, it is obvious that the trapping energy is much smaller. We simulated the trapping energy profile of particles and vesicles with different diameters, and show that the trapping energy of the VLPs is comparable with vesicles with the same diameter. The theoretical simulation method used here is Discrete Dipole Approximation (DDA), discussed in Section 2.2. First, we compare the following two models, (1) 110 nm diameter polystyrene spheres with refractive index 1.59 simulating the particles we used in Chapter 4; (2) 120 nm diameter vesicles with 10 nm lipid bilayer and refractive index 1.46 simulating the VLPs [44]. As a result, Fig. 5.8(a) and Fig. 5.8(b) show the comparison of the two models on the optical force profile in radial and axial direction, respectively; Fig. 5.8(c) and Fig. 5.8(d) show the difference on the trapping potential profile in radial and axial direction, respectively. The resulting trapping energies for the two models described above at the laser focus are 0.13 and 0.017 k_BT/mW respectively. The trapping energies of the two differ by a factor of 7.5.

Next, because the size of virus particles has large variation, we study the effect of the size on the trapping energy. Fig. 5.9(a) and Fig. 5.9(b) compare the optical force profile of vesicles with 100 nm to 140 nm in radial and axial direction respectively. Fig. 5.9(c) and Fig. 5.9(d) show the difference in trapping energy profile. For vesicles having a size 120 ± 20 nm, which reflects the sample we observed for VLPs, the trapping energy is $0.022 \pm 0.008 k_BT$ for each mW of laser power. This shows good agreement with the experimental results of the VLPs. Therefore, a modal of vesicles with the same thickness as the VLP lipid bilayer would be much more appropriate.

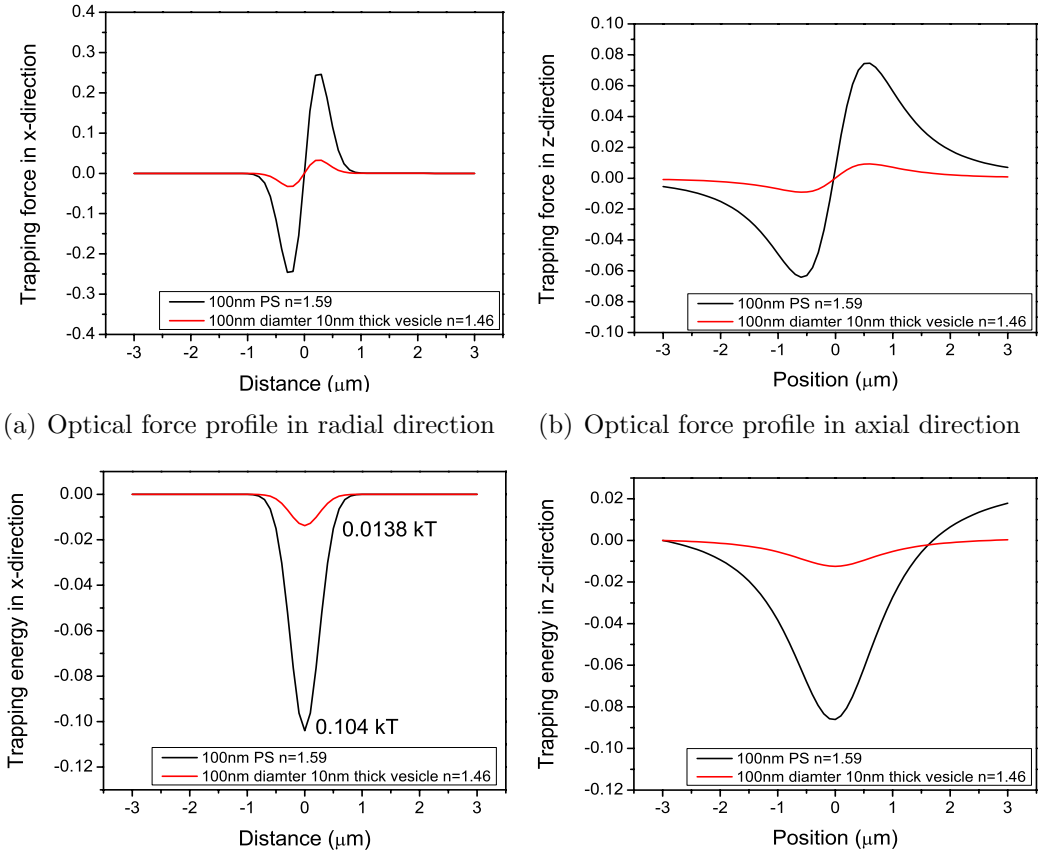

(a) Optical force profile in radial direction

(b) Optical force profile in axial direction

(c) Optical trapping energy profile in radial direction

(d) Optical trapping energy profile in axial direction

Figure 5.8: Comparison of the optical trapping force and trapping energy on 100 nm polystyrene spheres versus 10 nm thick vesicles with diameter 100 nm

Although the VLPs contain capsid and nucleo-capsid besides the membrane, the lipid bilayers of the VLPs dominate their optical properties.

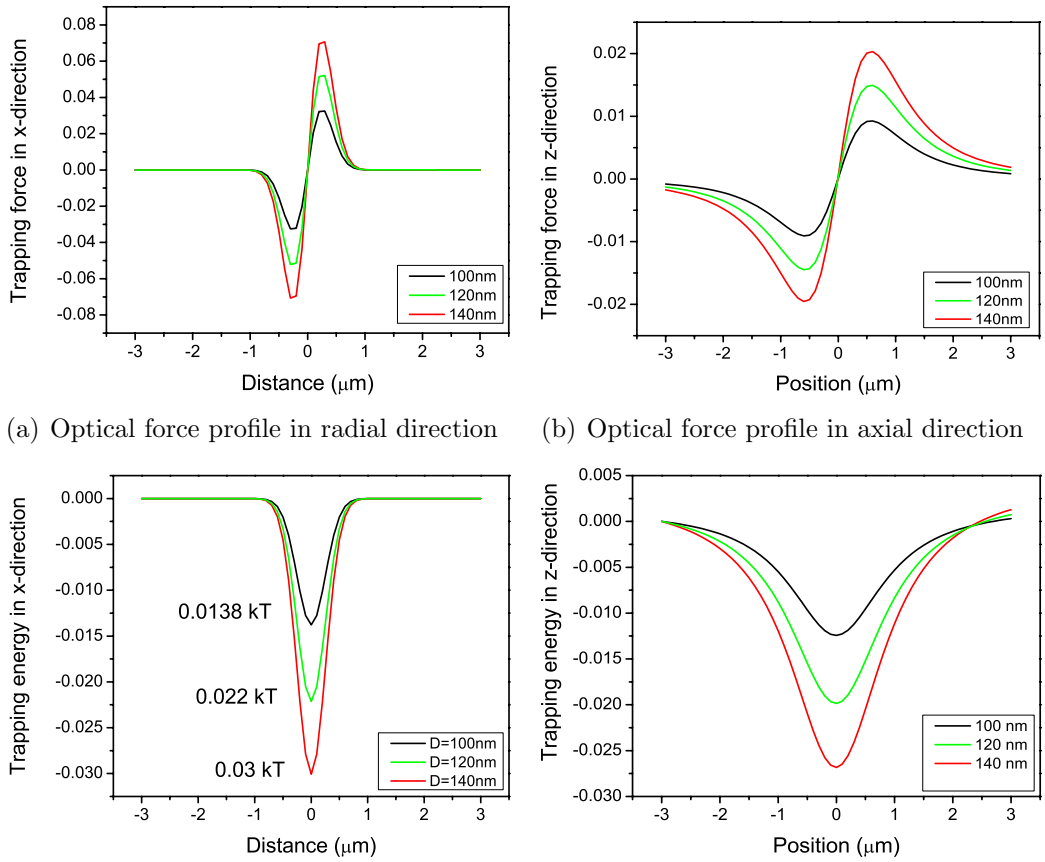

(a) Optical force profile in radial direction

(b) Optical force profile in axial direction

(c) Optical trapping energy profile in radial direction

(d) Optical trapping energy profile in axial direction

Figure 5.9: Comparison of the optical trapping force and trapping energy on 10 nm vesicles with diameters 100 nm, 120 nm and 140 nm respectively

5.3 Conclusions

We utilize FCS to quantitatively determine the concentration of HIV-1 virus-like-particles (VLPs) in an optical trap. We measured the trapping energy of each VLP and compared the resulting value of 0.02 k_BT for each mW of laser power to the theoretically derived results of 0.017 k_BT. It is anticipated that this result will be

useful in the characterization of viral particles such as HIV virus and Hepatitis A virus.

Chapter 6

Particle staining in a microfluidic chamber

Although revolutionized by the polymerase chain reaction (PCR) and related technologies for nucleic acid amplification, quantitative analysis of the circulating viral concentration, or viral load at the point of care (POC) remains challenging. Nowhere else is this more obvious than for diagnosis of HIV infections. Among the 25 million people who died as a result of HIV infection, and an additional 33 million currently infected individuals, a large part are from sub-Saharan Africa due to the lack of affordable, appropriate laboratory diagnostics [45, 46]. Thus, a compact and routine-operating point-of-care (POC) solution for quantitative viral detection remains an urgent public health priority, for both developed and developing counties.

New methods are emerging that directly detect and enumerate intact viruses, based on recent advances in optics, microfabrication, and nanotechnology [39–41].

Compared to molecular detection of viral fingerprints, whole particle viral detection has significant advantages in simple sample-preparation and fast sample-to-assay time, thus holding great promise for bringing improvements to the speed, sensitivity, operability, and portability of viral diagnostics.

Among the optical detection methods, FCS is well established for measuring the concentration and diffusion behavior of molecules in a real time and self-calibrated fashion, enumerating fluorescent bio-nanoparticles by FCS is a novel application and presents challenges such as low concentration of target particles. In this chapter, I integrate FCS with a microfluidic sample-processing chip. I will show that using this opto-fluidic device, effective staining, dialysis, and enumeration of particles can be achieved.

6.1 Chamber design and packaging

The chamber consists of three parts, two identical micro-channels with structure shown in Fig. 6.1(a) and Fig. 6.1(b) made of PDMS on an SU8 mold, and a polycarbonate membrane with pore size 20 nm. PDMS and toluene are mixed at 1:1 ratio, and used as a glue for bonding [47]. Next, I coat on the inner surface of the channels with the glue, align the two channels perpendicularly with the membrane sandwiched in the middle (as shown in Fig. 6.1(c), then bake overnight at temperature $140°C$ so that the toluene evaporates. The bars in the channels serve as supporting bridges for the chamber, and also to increase the bonding area. The assembled chamber is shown in Fig. 6.1(d). Depending on the openings of the four outlets, the direction of the flow in the chamber, either perpendicular or tangential

to the membrane, can be controlled.

6.2 On-chip particle staining

The particle staining is achieved via the binding between the biotin-labeled particles and streptavidin conjugated dye molecules. The binding of biotin to streptavidin is one of the strongest non-covalent interactions, and therefore commonly used in molecular biology and bionanotechnology. For a biotin labeled particle with diameter $200\,nm$ closely packed with streptavidin ($60\,kDa$), a maximum occupation number of 10000 streptavidin can be achieved. Without knowning the concentration of the particle, it is difficult to control the concentration of the streptavidin molelcules. Therefore, direct mixing the particle with streptavidin commonly leads to two outcomes: (1) excessive streptavidin molecules thus dye molecules in the solution; (2) particles not fully labeled due to the lack of streptavidin molecules. For FCS measurements, both results would lead to a low signal-to-noise ratio, as the first one has a high background fluorescent intensity, and the second one results in low signal. This device has an advantage in the control of the dye molecule concentration in both the labeling process and the detection process.

Fig. 6.2 schematically illustrates the diffusion of streptavidin conjugated dye molecules through the membrane with $20\,nm$ pores. The bottom channel is initally filled with biotin labeled particles, and the outlets are sealed to prevent evaporation and leakage. Next, Alexa 488 conjugated steptavidin is injected into the top channel and the fluorescent intensity in the bottom channel is monitered. Due to the concentration gradient of streptavidin molecules on the two sides of the membrane, the streptavidin diffuses through the membrane to the bottom channel until the concentration reaches equilibrium on both sides, shown in Fig. 6.3. Fig. 6.4 shows the time dependent intensity profile in the bottom channel.

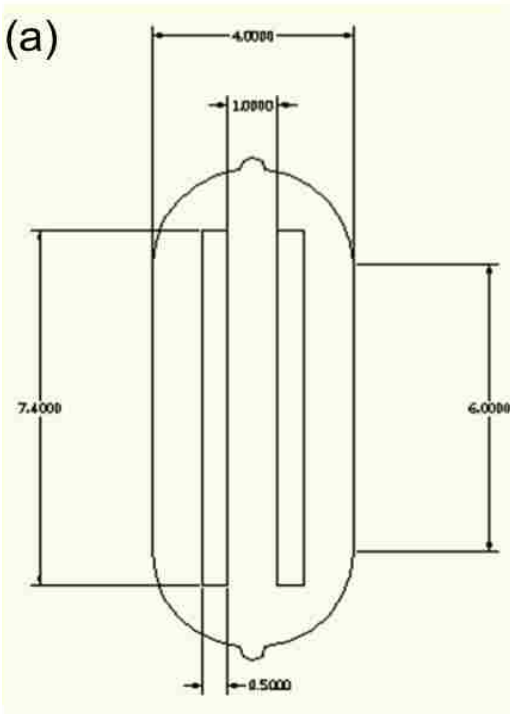

(a) Design of the mask

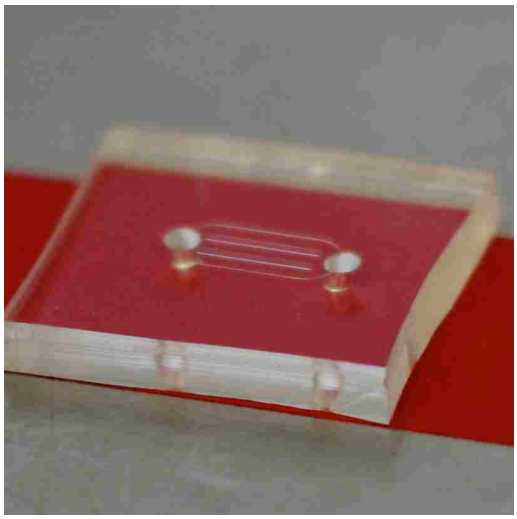

(b) A photo of the channel

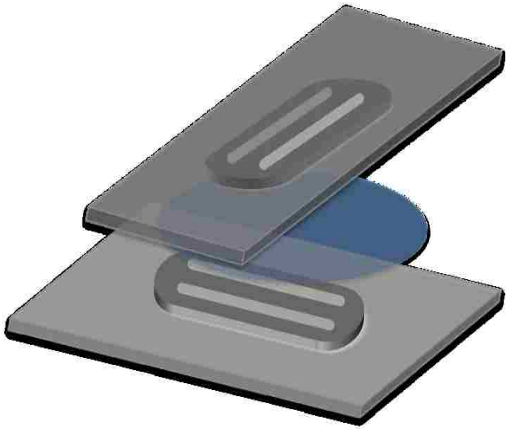

(c) Illustration of membrane packaging

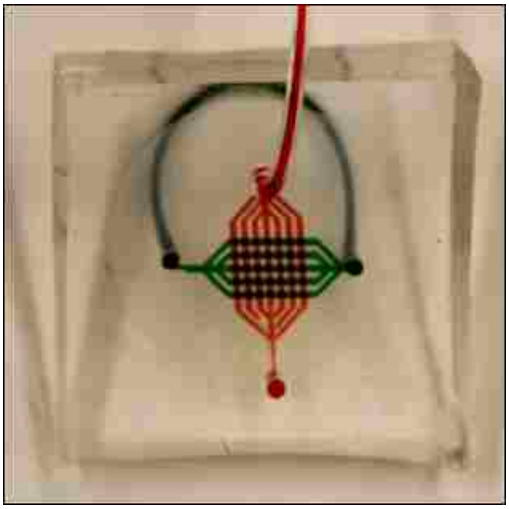

(d) A photo of the device

Figure 6.1: Chamber design and packaging

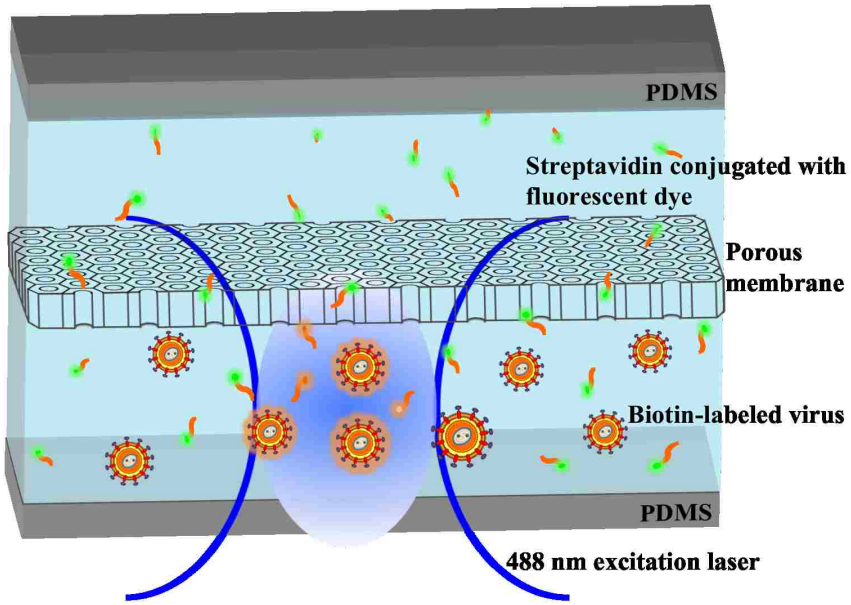

Figure 6.2: Molecule diffusion in the microfluidic device

After 1 hour for the chemical interaction between biotin and streptavidin, buffer solution is injected into the top channel continuously. Because of the reversal of the concentration gradient of streptavidin molecules on both sides of the membrane, the molecules will diffuse from the bottom channel back to the top channel. Hense, the fluorescence intensity in the bottom channel drops, indicating that the most of the excess un-labeled molecules are removed from the bottom channel, the background fluorescent intensity is therefore greatly reduced. As a result, the labeled particles stands out clearly from the background, shown in Fig. 6.5.

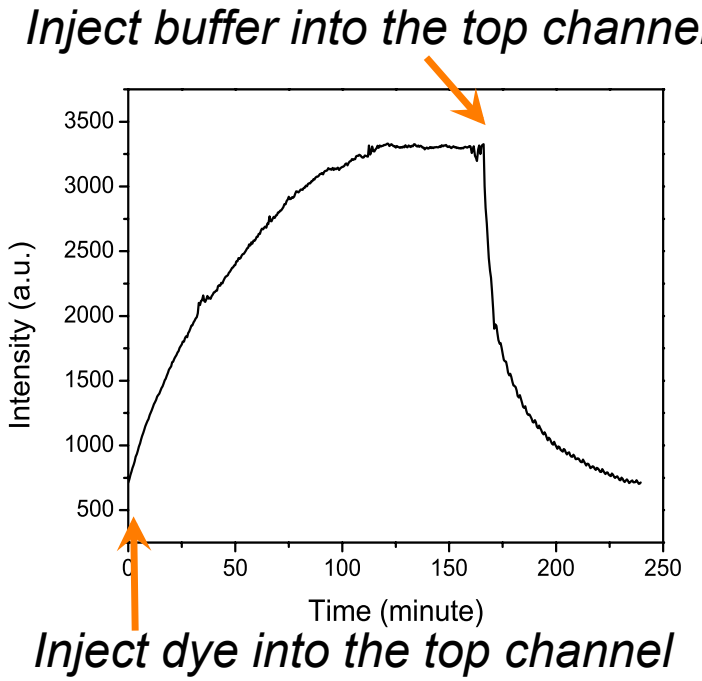

Figure 6.3: Time dependence of the fluorescence intensity in the bottom channel as dye molecules or buffer solution flow through the top channel.

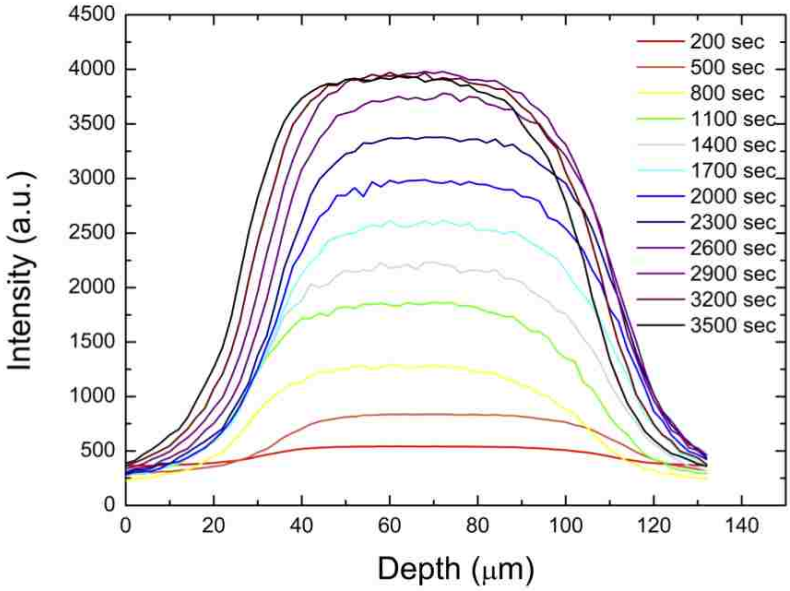

Figure 6.4: The time-dependent depth profile of the fluorescence intensity in the bottom channel.

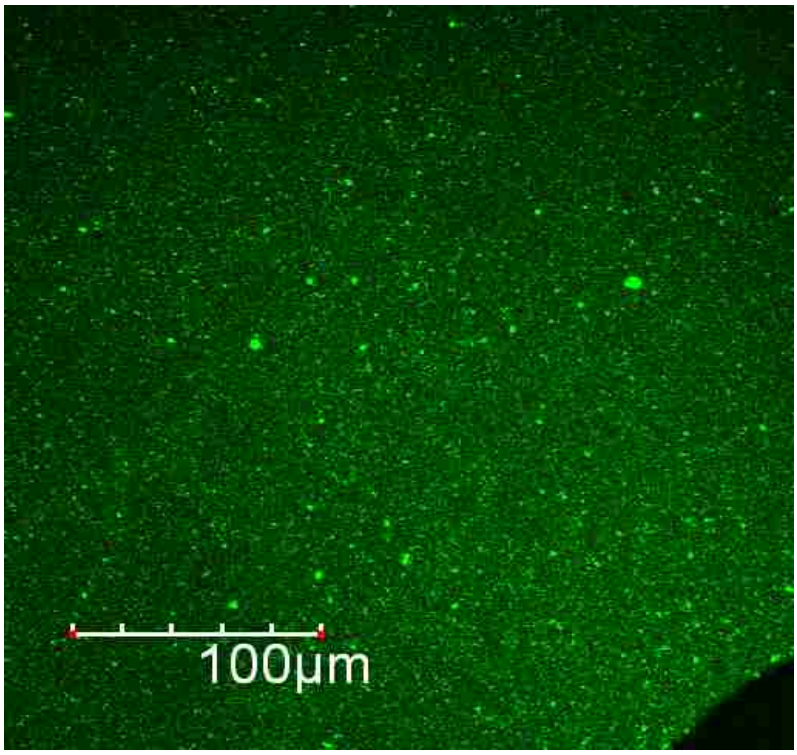

Figure 6.5: Fluorescence image of biotin-labeled particles stained in the micro-fluidic device with fluorescent dye.

6.3 Concentration measurements with low NA objectives

A critical issue in FCS is to discriminate the fluctuating signal from the noise, which requires simultaneously high fluorescence count rates per molecule (CRM) and low background. Therefore, FCS is commonly implemented on a confocal microscope with an immersion objective, providing high resolution and brightness. To ensure accurate measurements, a minimum sampling population of 1000 events is required.

The event rate for stationary process can be described as:

$$\frac{dN_S}{dt} = 4\pi w_0 DcN_A \tag{6.1}$$

where w_0 is the beam waist of the observation volume, D is the diffusion coefficient of the species in buffer solution, c is the concentration in molarity and N_A is the Avogadro constant.

Therefore, the small observation volume due to the implement of high NA objective sets a limit to the concentration range of FCS. To measure low species concentration, one can either elongate the sampling time, or enlarge sample volume by changing to a lower NA objective. Since the observation volume V_{eff} scales proportionally to $1/NA^4$ [48], Fchanging objectives, for example, from $NA = 1.3$ to 0.6 would increase the observation volume by a factor of 22, thus decrease the limit of FCS concentration range by the same order. However, the trade-off is the signal-to-noise ratio (S/N) decreases with the numerical aperture.

The signal-to-noise (S/N) ratio directly affects the accuracy of the FCS autocorrelation function. High background noise and low S/N ratio would lead to an overestimation of the number density. This is essential for biological applications, particularly in this experiment for two reasons:

(1) During the particle staining process, the unlabeled free dye molecule in the solution would significantly increase the background photon counts in FCS experiments.

(2) Dry objectives with long working distance commonly have low numerical apertures. Therefore the observation volume is much larger compared to the typical

FCS experiment with high numerial aperture. This will result in an increase of background noise due to Rayleigh and Raman scattering from the buffer solution, as well as a decrease of excitation intensity and collection efficiency, causing a low count rate per molecule.

Overall, this will lead to an overestimation of the particle number in the observation volume. The measured correlation function amplitude $G(0)$ needs to be scaled by $\langle F(t)\rangle^2 / \langle F(t) - F_{BG}\rangle$ where F_{BG} is the average background photocount [49].

In this experiment, a dry objective with $NA = 0.6$ is used. The particles are coated with biotin, and have intrinsic green fluorescence with excitation at $488\,nm$. The dye molecules Alexa 546 are conjugated with streptavidin molecules which bind steadily with biotin once they are less than 20 nm apart and would emit fluorescence with the excitation at 543 nm. According to these specifications, we adjusted our setup as shown in Fig. 6.6, with a confocal system consisting two lasers at wavelength $488\,nm$ and $543\,nm$.

The photocount signal and the FCS autocorrelation function of particles before and after staining is shown in Fig. 6.7. The black curve in Fig. 6.7(b) shows the ACF of the original fluorescence from the particle before staining, while the red curve shows the ACF of the signal from dye molecules after the staining and dialysis process. The two curves show good agreement.

Next, a serial dilution of the biotin labeled particles is prepared, stained in the device described before, and measured via FCS. Fig. 6.8 shows that the $\langle N\rangle$ before staining (black circles) and after staining (blue squares) changes linearly with the number density of the particles suspension. A linear relation is observed in Fig. 6.8, verifying the effectiveness of the staining and enumeration of the particles.

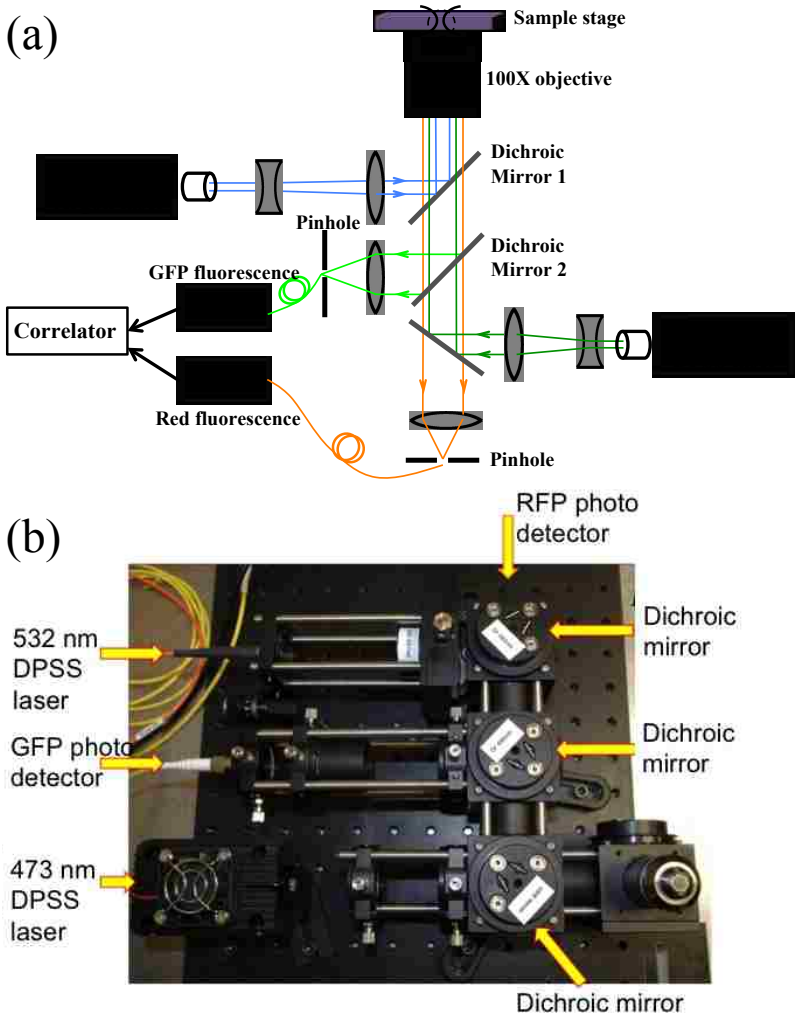

Figure 6.6: (a) Illustration of an optical system containing two excitation lasers. (b) Photograph of the optical setup.

6.4 Conclusions

In this chapter, I developed a technique using a sample-processing chip to label biotin-labeled viral particles with fluorescent dye molecules conjugated with streptavidin, and dialyzed the sample to significantly reduce the background signal. I then used FCS with low NA objective to quantitatively measure the concentration of the

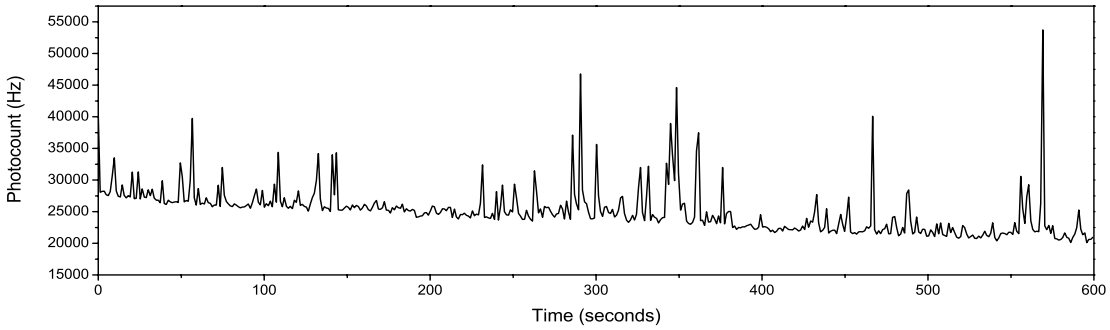

(a) Photocount signal after particle staining, measured in a chamber.

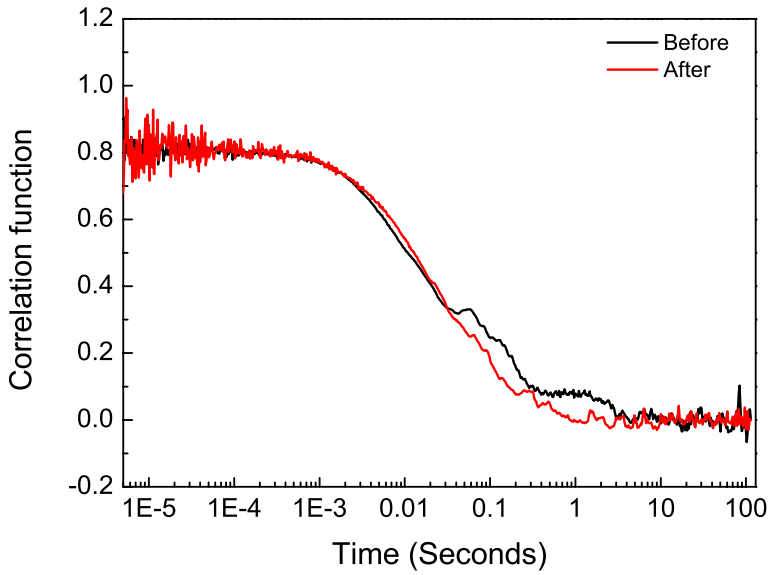

(b) The black curve is the FCS correlation function measured in the micro-fluidic device before the staining process using excitation laser at wavelength 488nm; the red curve is the correlation function of stained particles using excitation laser at wavelength 543nm.

Figure 6.7: FCS for stained particles

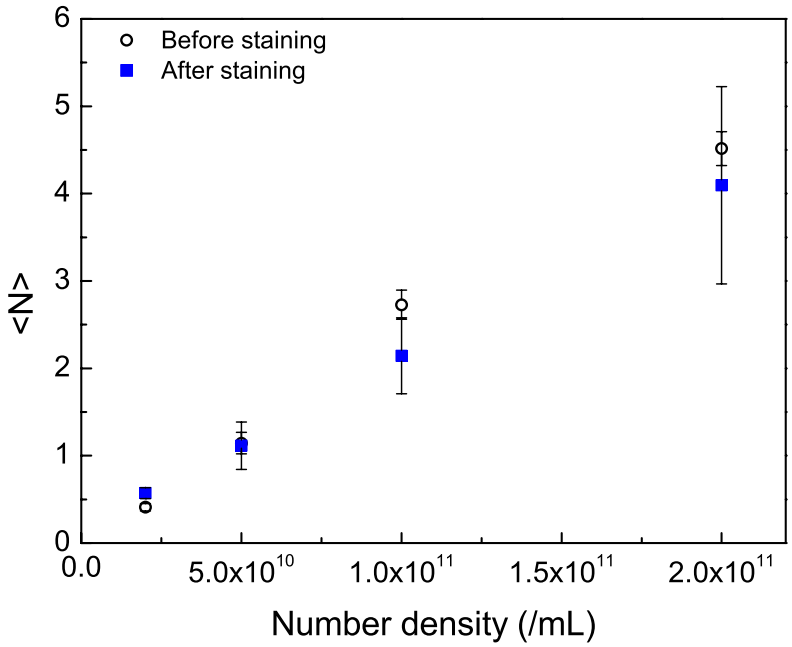

Figure 6.8: $\langle N \rangle$ measured before (white circles, with excitation laser 488nm) and after (blue squares, with excitation laser 543nm) particle staining process. A linear relationship indicates the system has been well calibrated.

virus. This technique enables direct and quantitative detection of bio-nanoparticle, which significantly reduces the sample-processing requirements and holds great potential for point-of-care applications.

Chapter 7

Concluding remarks and outlook

This work addresses the theoretical and experimental issues that one needs to deal with when using FCS to analyze colloidal nanoparticles in an optical trap.

How optical trapping of nanoparticles affects the FCS analysis has been an open question for a long time. Since there is no analytical expression for the FCS correlation function for particles in a Gaussian potential introduced by an optical trap, a harmonic potential was used instead to calculate the correlation function. The result of this calculation shows that the initial amplitude of FCS correlation function is inversely proportional to the mean particle number in the observation volume ($G(0) = 1/\langle N \rangle$). Experimentally, this relationship holds true for particles in a Gaussian potential with trapping energies as high as $6\,k_B T$. For higher trapping energies, $G(0) < 1/\langle N \rangle$, presumably because the probability of finding a particular particle with such a potential energy in the observation volume is no longer significantly lower than 1, thus it breaks the applicability of the Poisson statistics.

How $G(0)$ is affected by the Coulomb repulsion between colloidal charged particles in suspension also needs to be addressed. We used the grand canonical ensemble method to develop a general expression of $G(0)$ with consideration of particle interactions. The newly derived expression shows that $G(0)$ is a function of the temperature, the observation volume, and the colloidal osmotic compressibility. For colloidal particles in an optical trap, even when the ambient concentration of nanoparticles is low, the optical trapping will locally increase its concentration, making particle interaction non-negligible. Clearly, both the presence of optical trapping and, hence, increased particle interactions, affect how FCS should be used to analyze the statistics of optically confined nanoparticles.

With the fundamental issues resolved for polystyrene nanospheres, we were able to use FCS to determine the concentration of a dilute suspension of HIV-1 virus-like particles (VLPs) in an optical trap. The trapping energy of the VLPs was found to be $0.02\,k_BT$ per milliwatt of the trapping laser power. At the same time, a theoretical estimation of the trapping energy using discrete dipole approximation, for particles that are similar in properties to the VLPs, was in good agreement with the results obtained experimentally.

Motivated by the necessity of whole-particle viral sensing for point-of-care applications, an integrated opto-fluidic device that fluorescently labels bio-particles for FCS detection has been designed and constructed. In addition, by utilizing low-numerical-aperture objectives in the absence of optical trapping, we were able to extend the detection limit of FCS for the enumeration of the bio-nanoparticles.

With the framework established here for using FCS to analyze colloidal particles in the presence of optical trapping and particle interactions, this work extends the

applicability of virus sensing techniques to situations where other concentrating methods, such as electrophoresis or magnetic tweezers, have to be used.

Bibliography

[1] Morgan, H. & Green, N. G. Dielectrophoretic manipulation of rod-shaped viral particles. *Journal of Electrostatics* **42**, 279 – 293 (1997). URL http://www.sciencedirect.com/science/article/pii/S0304388697001599.

[2] Hughes, M. P., Morgan, H. & Rixon, F. J. Dielectrophoretic manipulation and characterization of herpes simplex virus-1 capsids. *European Biophysics Journal* **30**, 268–272 (2001). URL http://dx.doi.org/10.1007/s002490100144. 10.1007/s002490100144.

[3] Zheng, L., Brody, J. P. & Burke, P. J. Electronic manipulation of dna, proteins, and nanoparticles for potential circuit assembly. *Biosensors and Bioelectronics* **20**, 606 – 619 (2004). URL http://www.sciencedirect.com/science/article/pii/S0956566304001484. ¡ce:title¿Optical Biosensing¡/ce:title¿.

[4] Zhang, C., Khoshmanesh, K., Mitchell, A. & Kalantar-zadeh, K. Dielectrophoresis for manipulation of micro/nano particles in microfluidic systems. *Analytical and Bioanalytical Chemistry* **396**, 401–420 (2010).

URL http://dx.doi.org/10.1007/s00216-009-2922-6. 10.1007/s00216-009-2922-6.

[5] Neuman, K. C. & Nagy, A. Single-molecule force spectroscopy: optical tweezers, magnetic tweezers and atomic force microscopy. *Nat Meth* **5**, 491–505 (2008). URL http://dx.doi.org/10.1038/nmeth.1218.

[6] Yan, J., Skoko, D. & Marko, J. F. Near-field-magnetic-tweezer manipulation of single dna molecules. *Phys. Rev. E* **70**, 011905 (2004). URL http://link.aps.org/doi/10.1103/PhysRevE.70.011905.

[7] Ashkin, A. History of optical trapping and manipulation of small-neutral particle, atoms, and molecules. *Selected Topics in Quantum Electronics, IEEE Journal of* **6**, 841 –856 (2000).

[8] Grom, F., Kentsch, J., Muller, T., Schnelle, T. & Stelzle, M. Accumulation and trapping of hepatitis a virus particles by electrohydrodynamic flow and dielectrophoresis. *ELECTROPHORESIS* **27**, 1386–1393 (2006). URL http://dx.doi.org/10.1002/elps.200500416.

[9] Kolivoska, V. *et al.* Electrophoresis on a microfluidic chip for analysis of fluorescence-labeled human rhinovirus. *ELECTROPHORESIS* **28**, 4734–4740 (2007). URL http://dx.doi.org/10.1002/elps.200700397.

[10] Ashkin, A., Dziedzic, J. M., Bjorkholm, J. E. & Chu, S. Observation of a single-beam gradient force optical trap for dielectric particles. *Opt. Lett.* **11**, 288–290 (1986). URL http://ol.osa.org/abstract.cfm?URI=ol-11-5-288.

[11] Junio, J., Ng, J., Cohen, J. A., Lin, Z. & Ou-Yang, H. D. Ensemble method to measure the potential energy of nanoparticles in an optical trap. *Opt. Lett.* **36**, 1497–1499 (2011). URL http://ol.osa.org/abstract.cfm?URI=ol-36-8-1497.

[12] Wu, P., Huang, R., Tischer, C., Jonas, A. & Florin, E.-L. Direct measurement of the nonconservative force field generated by optical tweezers. *Phys. Rev. Lett.* **103**, 108101 (2009). URL http://link.aps.org/doi/10.1103/PhysRevLett.103.108101.

[13] Magde, D., Elson, E. & Webb, W. W. Thermodynamic fluctuations in a reacting system—measurement by fluorescence correlation spectroscopy. *Phys. Rev. Lett.* **29**, 705–708 (1972).

[14] Elson, E. L. & Magde, D. Fluorescence correlation spectroscopy. i. conceptual basis and theory. *Biopolymers* **13**, 1–27 (1974). URL http://dx.doi.org/10.1002/bip.1974.360130102.

[15] Hess, S. T., Huang, S., Heikal, A. A. & Webb, W. W. Biological and chemical applications of fluorescence correlation spectroscopy: a review. *Biochemistry* **41**, 697–705 (2002). URL http://pubs.acs.org/doi/abs/10.1021/bi0118512. PMID: 11790090, http://pubs.acs.org/doi/pdf/10.1021/bi0118512.

[16] Krichevsky, O. & Bonnet, G. Fluorescence correlation spectroscopy: the technique and its applications. *Reports on Progress in Physics* **65**, 251– (2002). URL http://stacks.iop.org/0034-4885/65/i=2/a=203.

[17] Thompson, N., Lieto, A. & Allen, N. Recent advances in fluorescence correlation spectroscopy. *Current Opinion in Structural Biology* **12**, 634–641 (2002).

[18] Kohler, R., Schwille, P., Webb, W. & Hanson, M. Active protein transport through plastid tubules: velocity quantified by fluorescence correlation spectroscopy. *Journal of Cell Science* **113**, 3921–3930 (2000). URL http://jcs.biologists.org/content/113/22/3921.abstract. http://jcs.biologists.org/content/113/22/3921.full.pdf+html.

[19] Banks, D. S. & Fradin, C. Anomalous diffusion of proteins due to molecular crowding. *Biophys J* **89**, 2960–2971 (2005). URL http://linkinghub.elsevier.com/retrieve/pii/S0006349505729404.

[20] Widengren, J., Rigler, R. & Mets, . Triplet-state monitoring by fluorescence correlation spectroscopy. *Journal of Fluorescence* **4**, 255–258 (1994). URL http://dx.doi.org/10.1007/BF01878460. 10.1007/BF01878460.

[21] Johnson, J., Chen, Y. & Mueller, J. D. Characterization of brightness and stoichiometry of bright particles by flow-fluorescence fluctuation spectroscopy. *Biophysical Journal* **99**, 3084–3092 (2010). URL http://www.sciencedirect.com/science/article/pii/S0006349510010532.

[22] Osborne, M. A., Balasubramanian, S., Furey, W. S. & Klenerman, D. Optically biased diffusion of single molecules studied by confocal fluorescence microscopy. *The Journal of Physical Chemistry B* **102**, 3160–3167 (1998). URL http://pubs.acs.org/doi/abs/10.1021/jp9715078. http://pubs.acs.org/doi/pdf/10.1021/jp9715078.

[23] Hosokawa, C., Yoshikawa, H. & Masuhara, H. Cluster formation of nanoparticles in an optical trap studied by fluorescence correlation spectroscopy. *Phys. Rev. E* **72**, 021408 (2005).

[24] Wang, J. *et al.* Brownian diffusion of gold nanoparticles in an optical trap studied by fluorescence correlation spectroscopy. *Laser Physics* **21**, 130–136 (2011). URL `http://dx.doi.org/10.1134/S1054660X1101021X`. 10.1134/S1054660X1101021X.

[25] Ito, S., Toitani, N., Yamauchi, H. & Miyasaka, H. Evaluation of radiation force acting on macromolecules by combination of brownian dynamics simulation with fluorescence correlation spectroscopy. *Phys. Rev. E* **81**, 061402 (2010).

[26] Meng, F. & Ma, H. Fluorescence correlation spectroscopy analysis of diffusion in a laser gradient field: a numerical approach. *J. Phys. Chem. B* **109**, 5580–5585 (2005). URL `http://dx.doi.org/10.1021/jp044898g`.

[27] Davis, T. J. Brownian diffusion of nano-particles in optical traps. *Opt. Express* **15**, 2702–2712 (2007). URL `http://www.opticsexpress.org/abstract.cfm?URI=oe-15-5-2702`.

[28] Ling, L., Zhou, F., Huang, L. & Li, Z.-Y. Optical forces on arbitrary shaped particles in optical tweezers. *Journal of Applied Physics* **108**, 073110 –073110–8 (2010).

[29] Haustein, E. & Schwille, P. Fluorescence correlation spectroscopy: Novel variations of an established technique. *Annual Review of Biophysics and Biomolecular Structure* **36**, 151–169 (2007).

[30] Schwille, P., Haupts, U., Maiti, S. & Webb, W. W. Molecular dynamics in living cells observed by fluorescence correlation spectroscopy with one- and two-photon excitation (1999). URL http://linkinghub.elsevier.com/retrieve/pii/S0006349599770657.

[31] Kim, S. A., Heinze, K. G. & Schwille, P. Fluorescence correlation spectroscopy in living cells. *Nat Meth* **4**, 963–973 (2007). URL http://dx.doi.org/10.1038/nmeth1104.

[32] Qian, H. & Elson, E. L. Analysis of confocal laser-microscope optics for 3-d fluorescence correlation spectroscopy. *Appl. Opt.* **30**, 1185–1195 (1991). URL http://ao.osa.org/abstract.cfm?URI=ao-30-10-1185.

[33] Rigler, R., Mets, ., Widengren, J. & Kask, P. Fluorescence correlation spectroscopy with high count rate and low background: analysis of translational diffusion. *European Biophysics Journal* **22**, 169–175 (1993). URL http://dx.doi.org/10.1007/BF00185777. 10.1007/BF00185777.

[34] Hess, S. T. & Webb, W. W. Focal volume optics and experimental artifacts in confocal fluorescence correlation spectroscopy (2002). URL http://linkinghub.elsevier.com/retrieve/pii/S0006349502739908.

[35] Wu, B., Chen, Y. & Mller, J. D. Fluorescence correlation spectroscopy of finite-sized particles. *Biophysical Journal* **94**, 2800–2808 (2008). URL http://www.sciencedirect.com/science/article/pii/S0006349508705319.

[36] Junio, J., Park, S., Kim, M.-W. & Ou-Yang, H. D. Optical bottles: A quantitative analysis of optically confined nanoparticle ensembles in suspension. *Solid*

State Communications **150**, 1003 – 1008 (2010). Nanoscale Interfacial Phenomena in Complex Fluids.

[37] Hosokawa, C., Yoshikawa, H. & Masuhara, H. Optical assembling dynamics of individual polymer nanospheres investigated by single-particle fluorescence detection. *Phys. Rev. E* **70**, 061410 (2004).

[38] Abney, J., Scalettar, B. & Hackenbrock, C. On the measurement of particle number and mobility in nonideal solutions by fluorescence correlation spectroscopy (1990). URL `http://linkinghub.elsevier.com/retrieve/pii/S0006349590823717`.

[39] Cheng, X., Chen, G. & Rodriguez, W. Micro- and nanotechnology for viral detection. *Analytical and Bioanalytical Chemistry* **393**, 487–501 (2009). URL `http://dx.doi.org/10.1007/s00216-008-2514-x`. 10.1007/s00216-008-2514-x.

[40] Huh, D., Gu, W., Kamotani, Y., Grotberg, J. B. & Takayama, S. Microfluidics for flow cytometric analysis of cells and particles. *Physiological Measurement* **26**, R73 (2005). URL `http://stacks.iop.org/0967-3334/26/i=3/a=R02`.

[41] Liu, W.-T. *et al.* Microfluidic device as a new platform for immunofluorescent detection of viruses. *Lab Chip* **5**, 1327–1330 (2005). URL `http://dx.doi.org/10.1039/B509086E`.

[42] Chen, Y., Wu, B., Musier-Forsyth, K., Mansky, L. M. & Mueller, J. D. Fluorescence fluctuation spectroscopy on viral-like particles reveals variable gag stoichiometry. *Biophysical Journal* **96**, 1961–1969 (2009). URL http://www.sciencedirect.com/science/article/pii/S0006349509000204.

[43] Shevchuk, A. I. *et al.* Imaging single virus particles on the surface of cell membranes by high-resolution scanning surface confocal microscopy. *Biophys J* **94**, 4089–4094 (2008). URL http://linkinghub.elsevier.com/retrieve/pii/S0006349508704089.

[44] Fuller, S. D., Wilk, T., Gowen, B. E., Kr?usslich, H.-G. & Vogt, V. M. Cryo-electron microscopy reveals ordered domains in the immature hiv-1 particle. *Curr Biol* **7**, 729–738 (1997). URL http://linkinghub.elsevier.com/retrieve/pii/S0960982206003319.

[45] Petti, C. A., Polage, C. R., Quinn, T. C., Ronald, A. R. & Sande, M. A. Laboratory medicine in africa: A barrier to effective health care. *Clinical Infectious Diseases* **42**, 377–382 (2006). URL http://cid.oxfordjournals.org/content/42/3/377.abstract. http://cid.oxfordjournals.org/content/42/3/377.full.pdf+html.

[46] Gilks, C. F. *et al.* The who public-health approach to antiretroviral treatment against hiv in resource-limited settings. *The Lancet* **368**, 505 – 510 (2006). URL http://www.sciencedirect.com/science/article/pii/S0140673606691587.

[47] Chueh, B.-h. *et al.* Leakage-free bonding of porous membranes into layered microfluidic array systems. *Analytical Chemistry* **79**, 3504–3508 (2007). URL http://pubs.acs.org/doi/abs/10.1021/ac062118p. http://pubs.acs.org/doi/pdf/10.1021/ac062118p.

[48] Wenger, J., Gerard, D., Aouani, H. & Rigneault, H. Disposable microscope objective lenses for fluorescence correlation spectroscopy using latex microspheres. *Analytical Chemistry* **80**, 6800–6804 (2008). URL http://pubs.acs.org/doi/abs/10.1021/ac801016z. PMID: 18681458, http://pubs.acs.org/doi/pdf/10.1021/ac801016z.

[49] Starchev, K., Ricka, J. & Buffle, J. Noise on fluorescence correlation spectroscopy. *Journal of Colloid and Interface Science* **233**, 50–55 (2001). URL http://www.sciencedirect.com/science/article/pii/S0021979700972291.

Vita

Education

Lehigh University, Ph.D., Department of Physics, GPA: 3.85, Sep 2012

Lehigh University, M.S., Department of Physics, GPA: 3.85, Jan 2010

University of Science and Technology of China, B.S., Department of Modern Physics, GPA: 3.3 Jul 2007

Skills

Optics

Optical workbench design and alignment; Confocal microscope operation and maintenance; Optical trapping; Fluorescence correlation spectroscopy (FCS); Raman spectroscopy; UV-Vis spectroscopy; Dynamic light scattering (DLS); Surface Plasmon Resonance (SPR); Atomic force microscopy (AFM).

Materials

Microfluidic devices design and development; MEMS design and development; Photolithograph; Evaporative deposition; Wet etching; Spin coating; SEM; Oxygen plasma cleaning, carbon nanotube.

Biological science

Cell, bacterial and yeast culture; DNA extraction, purification and quantification; Bacteria transformation; Cell transfection; Viral infectivity assay; ELISA.

Computer skills

Origin, SolidWorks, COMSOL, Mathematica, LabView, AutoCAD, LaTeX, Microsoft Office.

Leadership and activities

- Selected as the student representative of Lehigh University to the New York Academy of Science Condensed Matter Group. (Sep 2011 - present)
- Coordinated with representatives from twelve universities and organizations to bring together the 6th Gotham Metro Condensed Matter Meeting, which provided an opportunity for sharing research and networking with fellow physicists. (Sep 2011 - present)
- Supervised and trained undergraduate students in research field for over two years. (May 2009 - present)

- Taught undergraduate courses Electricity and Magnetism and Introductory Physics. (Sep 2007 - May 2012)

Publications

1. "Fluorescence correlation spectroscopy of interacting colloidal particles in optical confinement." Y. Hu, X. Cheng and H. D. Ou-Yang, *in preparation*

2. "Enumerating HIV-1 virus-like particles in a gradient potential." Y. Hu, X. Cheng and H. D. Ou-Yang, *in preparation*

3. "Fluorescence correlation spectroscopy in a microfluidic chip for viral whole particle enumeration." Y. Hu, B. Wang, P. Soto, H. D. Ou-Yang and X. Cheng, *in preparation*

4. "Fluorescence correlation spectroscopy in an optical trap." Y. Hu, X. Cheng and H. D. Ou-Yang, Proc. SPIE, 7762, 776229, (2010)

Conference contributions

1. "Fluorescence correlation spectroscopy enumerates nanoparticles in an optical trap." Y. Hu, X. Cheng and H. D. Ou-Yang, APS March Meeting, 2012

2. "Direct enumeration of dilute bio-nanoparticles in an optical trap." Y. Hu, H. D. Ou-Yang and X. Cheng, BMES Meeting, 2011

3. "Fluorescence correlation spectroscopy revealing the statistics of nanoparticles in an optical trap." Y. Hu, X. Cheng and H. D. Ou-Yang, SPIE, 2011

4. "Poisson or not Poisson: Probability distribution of colloidal nanoparticles in an optical trap." Y. Hu, X. Cheng and H. D. Ou-Yang, APS March meeting, 2011

5. "'Fluorscence correlation spectroscopy in an optical trap." Y. Hu, X. Cheng and H. D. Ou-Yang, SPIE, 2010

6. "Fluorscence correlation spectroscopy in an optical trap," Y. Hu, X. Cheng and H. D. Ou-Yang, APS March meeting, 2010

7. "Self-diffusion of nanoparticles in a crowded environment", Y. Hu, X. Cheng and H. D. Ou-Yang, APS March meeting, 2010